12-2023

Viscosity of Adsorbent Slurries for Washcoating Applications

Nitish Chauhan
Florida Institute ofTechnology, nchauhan2016@my.fit.edu

VISCOSITY OF ADSORBENT SLURRIES FOR WASHCOATING APPLICATIONS

by

Nitish Chauhan

A thesis submitted to the Department of Mechanical and Civil Engineering of
Florida Institute of Technology
in partial fulfillment of the requirements
for the degree of

Master of Science
in
Mechanical Engineering

Melbourne, Florida
December 2023

We, the undersigned committee, hereby approve the attached thesis,
"VISCOSITY OF ADSORBENT SLURRIES FOR WASHCOATING APPLICATIONS."
by
Nitish Chauhan

_____

Darshan G. Pahinkar, Ph.D.
Assistant Professor
Mechanical and Civil Engineering
Major Advisor

_____

M. Toufiq Reza, Ph.D.
Associate Professor
Chemistry and Chemical Engineering

_____

Anand Balu Nellippallil, Ph.D.
Assistant Professor
Mechanical and Civil Engineering

_____

Ashok Pandit, Ph.D., P.E.
Professor and Department Head
Mechanical and Civil Engineering

Abstract

Title: VISCOSITY OF ADSORBENT SLURRIES FOR WASHCOATING APPLICATIONS

Author: Nitish Chauhan

Advisor: Darshan G. Pahinkar, Ph.D.

The viscosity of adsorbent slurries is pivotal in understanding their rheological behavior, yet, the research on adsorbent slurry viscosity has been limited. This study addresses this gap by analyzing porous and non-porous solutes' behavior in solvents and then applying it to the washcoating adsorbents on ceramic substrates. By examining MIL-101 (Cr), glass beads, silica nanoparticles, and titania, the study aims to comprehend the viscosity variations of each solute in the solvents, water and ethanol. A key observation from this study was the significant role of wetting in determining viscosity, as initial results found that MIL-101 (Cr) exhibited the highest viscosity in water-based slurries. In contrast, in ethanol slurry, glass beads exhibited the highest viscosity, which could be attributed to the low contact angle between ethanol and glass beads. Based on these and several more findings, a semi-empirical model was formulated using the Buckingham π theorem, which showed similar values for viscosity and was validated for up to 30% volume fraction. Moreover, shear thinning behavior was consistently observed across all experiments, which enhances the application based on these slurries.

To understand the polydisperse effects on slurry viscosity, a mixture slurry of MIL-101(Cr) and silica nanoparticles is analyzed, and then a novel approach is developed for washcoating metal-organic framework MIL-101 (Cr), a high-performance water adsorbent, uniformly on a cordierite honeycomb microchannel monolith. The methodology relies upon the characterization of the slurry, which consists of MIL-101 (Cr), SiO_2 nanoparticles binder, and a distilled water base and the adsorbent loading as its function. The adsorbent layer thickness is experimentally characterized as a function of viscosity and binder and MIL-101 (Cr) mass fraction. The highest normalized loading of 10%, at the optimized solid volume fraction of 19%, is identified, for which the layer thickness is remarkably high at 106 μm. The coated layers are analyzed for homogeneity, porosity, durability, and adsorbent property variations before and after coating through scanning electron microscopy, X-ray diffraction, Fourier transform infrared spectroscopy, and ultrasonic vibration tests. While the adsorbent properties were retained after the washcoating process, the adsorbent layer showed excellent adhesion and durability after ultrasonic vibrations for 4800 hours. The channels fabricated using this method can be readily scaled up in separation and heat pump systems.

Table of Contents

List of Figures

List of Tables

Acknowledgment

First and foremost, I would like to extend my deepest gratitude to my advisor, Dr. Darshan G. Pahinkar, whose unwavering support, guidance, and profound expertise have been invaluable throughout my journey. His dedication towards the research, meticulous approach to problem-solving, and immense patience has been instrumental in shaping this thesis. I am highly grateful to him for always being available, guiding me through my research, and creating an environment of open dialogue and constructive feedback. All this has motivated me to be more diligent and instilled a zeal for learning.

I would also like to thank my committee members, Dr. Anand Balu Nellippallil and Dr. Toufiq Reza, for agreeing to be on my committee; their insights, criticism, and feedback are invaluable to my work.

Finally, I would like to thank my family for their love and support throughout my journey.

1 Introduction

The current energy landscape is dominated by fossil fuel combustion, leading to environmental consequences that worsen each year [1]. Therefore, there is an urgent need to effectively utilize primary energy resources and develop devices and systems to utilize waste heat from this combustion. Thermally driven energy systems, such as adsorption heat pumps, can address these concerns; and offer additional advantages such as (a) a reduced number of moving parts, enhancing durability, (b) the option to use nontoxic, non-flammable, zero-Global Warming Potential (GWP) working fluids, such as water, (c) the ability to work with low-temperature heat sources, (d) flexible and passive operation, and (e) potential for low capital cost [2]. Such a transition will eventually contribute to a reduced burden on thermal power infrastructures, reduced use of conventional energy sources, and reduced carbon footprint, simultaneously achieving overall energy sufficiency.

However, existing embodiments of adsorption systems suffer from performance and scalability limitations; thus, significant improvements to the state-of-the-art are required. There are two major bottlenecks in terms of mass and heat transfer. The first is the widespread use of packed adsorbent beds, which results in poor mass transport, despite being easy to fabricate. These packed beds are large cylinders filled with adsorbent pellets ($\approx$ 5 mm size), creating porous structures. The gas diffusion and adsorption in these beds are sluggish, requiring long cycles.

Furthermore, electrically driven vacuum pumps are generally used to manipulate the thermodynamic state of these beds, which otherwise could be done by raising their temperature. However, such heat-driven adsorbent regeneration in packed beds is not favored because of the low thermal conductivity of the porous adsorbents, being the second issue. Coupled with the porous structure of the bed, rapid heating and cooling of the adsorbent becomes impractical [3, 4]. These two issues can be solved using adsorbent-coated microchannels (Figure 1), which provide excellent heat and mass transfer characteristics. Such design eliminates the flow resistance because dedicated flow passages and thin adsorbent layers result in rapid heat and mass exchange.

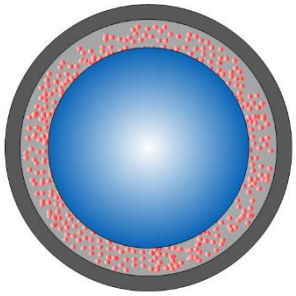

Figure 1: An Adsorbent Coated Channel (Blue – flow area, red – adsorbent particles, light gray – binder matrix, dark gray – substrate)

Earlier work conducted by Pahinkar et *al.* [1-3] showed that submillimeter-sized adsorbent-coated channels improve the capacity of the adsorption-based carbon dioxide (CO_2) separation systems by up to two orders of magnitude while maintaining the purity, recovery factors, and energy requirement of existing systems [5-8]. It was also reported that adsorption heat pumps could be improved significantly by using adsorbent-coated microchannels. At least two packed beds are usually required to produce continuous cooling in the case of

conventional systems, increasing the capital cost and footprint [4-6]. The adsorbent-coated microchannels are predicted to create an extreme asymmetry in the operation that allows the adsorption heat pump to produce near-continuous cooling using only one bed with a competitive primary energy coefficient of performance (COP_{PE}) with the existing systems [7]. These designs used silica gel as the adsorbent with a maximum uptake of 0.4 kg-water kg-ads^{-1}. However, adsorbents with higher adsorption capacity can significantly enhance this performance. A new class of adsorbents, Metal-Organic Framework (MOF), has been investigated in recent years and more specifically, MIL-101 (Cr) has been reported to adsorb up to 1.5 kg-water kg-ads^{-1} [8], thereby warranting the scaled-up experimental performance demonstration of such high-performance adsorption heat pumps using these adsorbents.

However, the methods to fabricate these coated microchannels are poorly characterized, and the current portfolio of adsorbent-coated microchannels shows a high variance in performance [9]. This variation and subsequent adsorption system underperformance are attributed to a lack of porosity and uniform distribution of the adsorbent [1]. In fact, the commercially available adsorbent-coated microchannels (also known as Porous Layer Open Tubular (PLOT) columns), which are conventionally used for gas chromatography and mass spectrometry applications, are expensive; however, they rarely have any adsorbent on their inner walls [1] (unlike the ideal scenario in Figure 1), while their claimed thickness could be as high as 30 μm. Therefore, if robust, porous and uniform adsorbent layers are fabricated on microchannel walls using a well-characterized and inexpensive technique, the significant disconnect between the predicted potential of these new high-performance water adsorbents [10] and their actual use in scalable adsorption heat pumps can be bridged.

Meanwhile, washcoating remains the most inexpensive and versatile method for structuring adsorbents, which requires preparing a slurry of appropriate viscosity using adsorbents, binder, additives, and solvents, dipping the substrates into the slurry, followed by quick drying. However, there is hardly any definitive research on how to achieve this viscosity as a function of integral parameters like solid volume fractions, adsorbent particle size, their physical properties, and most importantly, solvents wetting the adsorbent particles and themselves getting adsorbed. Surprisingly, no viscosity model exists for adsorbent slurries. *With these motivations, the thesis focuses on determining a unified semi-empirical viscosity model through extensive experiments and slurry rheology fundamentals and incorporating it into developing a versatile, in-situ washcoating method to fabricate adsorbent-coated microchannels for utility in adsorption heating and cooling systems*. The thesis has two primary goals:

Goal 1 – Unified viscosity model for adsorbent slurries: This goal will answer the fundamental questions:

1. *What are the typical characteristics of adsorbent slurries? What non-dimensional parameters govern the viscosity of adsorbent slurries? Can a unified viscosity model be developed using these parameters?*

This goal focuses on developing a unified semi-empirical model for the viscosity of adsorbent slurries, which takes into account adsorbent-solvent interaction, including wetting and adsorption, particle size, density, strain rate, volume fraction and liquid-solid contact angle. Non-dimensional numbers like Reynolds number will be determined using rheology fundamentals, and the obtained data from experiments will be processed in terms of them to

assist the model development. The scientific outcome for goal 1 is an experimentally validated unified model for the viscosity of adsorbent slurries as a function of integral factors accounting for the effect of adsorption and wetting.

Goal 2 – Porous adsorbent layer fabrication and performance demonstration: The fundamental questions that shall be answered through research toward this goal are:

1. *How can a porous adsorbent layer be achieved without using a pore-forming agent?*
2. *Does the washcoating process retain the properties of the adsorbent and provide adequate strength to the layer?*

These questions will be answered by developing an optimized washcoating process using the ideal slurry viscosity determined in the previous task. Here, the overall hypothesis is that water can replace the pore-forming agents (*e.g.,* starch), which are known to make the layers brittle. It will be tested through a combination of scanning electron microscopy (SEM), Energy Dispersive X-ray Spectroscopy (EDS), and nanoindentation tests to assert the porosity, homogeneity and strength of the layer for a *minimum target layer thickness* of 100 μm. Furthermore, reduced order computational models will be developed to characterize the relative kinetics of sensible heating of the adsorbent layer and desorption of solvent from the adsorbent that results in pore formation and drying of the layer. The scientific outcome for Goal 2 is an optimized washcoating process with the fewest degrees of freedom to produce a robust and porous layer.

The thesis, therefore, has four chapters in total. The second chapter details the experimental and analytical approach used in developing a unified model for the viscosity of adsorbent

slurries (Goal 1), whereas the third chapter details a washcoating method that uses the viscosity of these slurries and analyzes its effect on the washcoating performance (Goal 2). The thesis concludes with salient findings in Chapter 4.

2 Experiments for Slurry Rheology

2.1 Motivation

Viscosity is a crucial thermophysical property of any solvent – particulate mixture, which needs to be washcoated, as it decides the process time scale and particle retention amount. First, it must be understood how solvents like water form a mixture with any solid powder. For example, water forms perfectly homogeneous solutions with compounds like salt because these solids break down into ions of the size of the order of a few Angstroms due to attraction from polar water molecules until their solid appearance is gone [11]. For solids that cannot dissolve like this, distinct particles could be seen suspended in water because they cannot be further broken down into smaller particles. Note that while slurries or suspensions are the terms interchangeably used for mixtures of relatively large solid particles in a solvent (> 1 μm, like muddy water) that are prone to sedimentation, colloids are their subset for much smaller particles (<< 1 μm, like ink), which show resistance to sedimentation. The discussion on suspensions, slurries or colloids here is focused on solid particles in liquid solvents. However, using these terms for mixtures of other phases is common (*i.e.,* fog: liquid water droplets in the air). Several models are proposed for the viscosity of liquid-liquid mixtures [12, 13], whereas the slurry models are confined to solid non-interacting spheres in pure solvents [13]. Einstein proposed a model for the viscosity of suspensions of solid spheres in a solvent of viscosity μ (Eq.(1)) [14]; however, it is valid for a volume fraction φ less than 0.02 [15].

$$\mu_{mix} = \mu\left(1 + 2.5\varphi\right) \tag{1}$$

Many versions of this equation, including virial expansions, have been proposed for more concentrated slurries with particulate phases modeled as an effective medium or using viscous dissipation from them, offering a theoretical basis for such models. Many models consider the maximum packing fraction of solid particles in the liquid solvent ($\varphi_{\max}$), which is 0.637 for random spheres of the same size and increases to 0.74 for hexagons [16]. An example is shown in Eq. (2), which approaches Einstein's equation for $\varphi \rightarrow 0$ [17].

$$\mu_{mix} = \mu\left(1 - \varphi / \varphi_{\max}\right)^{-2.5\varphi_{\max}} \tag{2}$$

These models are valid for solid spheres that are not porous or exhibit affinity with each other or the liquid. Additionally, experimental validations reported for such models are specific to hard spheres [13, 18], again highlighting the need for viscosity models for more practical fluids such as inks or adsorbent slurries, where parameters beyond volume fractions play an essential role. Meanwhile, empirical viscosity models have their own space here due to the absence of broader theoretical models. A purely empirical viscosity model for solid spheres was proposed decades ago [19]; however, it lacks a basis to reveal interdependent phenomena resulting in a lack of applicability. The latest attempts to quantify the viscosity of suspensions of solid spheres using a semi-empirical approach and using solid fractions, maximum packing fractions and particle stiffness were inconclusive [20]. Additional inputs using the number of particles per length were found to assist with model refinement. However, they lacked a foundation for why only that factor was necessary [21].

This discussion is critical to establish two crucial literature gaps and the need for more research:

1. Whether theoretical or empirical, the entire literature on the viscosity of slurries is based on solid spheres in liquid solvents. These spheres are rigid, non-porous and may or may not have any affinity for the carrier liquid, which is not considered.
2. The viscosity of more complex fluids like adsorbent slurries is hypothesized to be heavily influenced by the solid volume fraction, particle size and shape, physical properties, interactions between liquid solvent and these particles like wetting, and strain rate [12]. *A valid viscosity model for adsorbent slurries of any type (empirical, semi-empirical or theoretical), which shows dependence on these factors, has not been heretofore proposed or demonstrated.*

2.2 Theoretical Background

The viscosity of slurries has always been shown to depend on the particulate volume fraction [12, 18]. Additional parameters that can be hypothesized to influence the slurry viscosity are particle size, density and shape, and strain rate. Particles within static slurries tend to coagulate; however, tentative formations of these particles break up, describing typical shear-thinning behavior when stirred. Longer, chainlike particles offer greater resistance to move than spherical particles because of their ability to form longer structures [22]. Heavy particles tend to settle or undergo sedimentation quickly, showing resistance to forming temporary bonds when sheared, while lighter particles stay within the medium, maintaining the viscosity. Dispersion of particles could be one of the factors; however, it is critical only

during early mixing when particles tend to spread out quickly due to the surface tension of the solvent pulling them apart. The dispersion may not have any influence in a uniformly homogenized slurry, where the particles are already inside the liquid solvent. While these parameters and their effects on the viscosity of the slurry are easy to comprehend, as such, such effects have never been collectively quantified using a unified model.

For adsorbent slurries, two more parameters influence the viscosity significantly. They are adsorption, which is the entry of the solvent into the nanopores of the particles, and simultaneous wetting (or non-wetting) of the adsorbent particles by the solvent, which can be characterized by the measurement of contact angles. These effects could be combined into suitable non-dimensional numbers to develop a unified model for the viscosity of adsorbent slurries.

The conventional understanding of adsorption is that an adsorbent preferentially attracts an adsorbate from its 'gaseous' phase and then stores it at a high density inside the micro/nanopores. This high density depends on the partial pressure of the gaseous adsorbate and the temperature of the adsorbent. While this principle is ubiquitous for all adsorption applications, it may not hold when the adsorbate is already liquid, and a phase change for adsorption purposes is not even necessary. The liquid adsorbate, the solvent in the case of the washcoating slurry, will still enter the nanopores, provided the solid adsorbent particles allow such entry, being solvent'philic'. This liquid adsorbate 'wetting' the solid adsorbent and entering it is not fully understood and characterized. If the solvent can wet the solute particles, the slurry will likely stay in its form longer [23]. In contrast, if the solvent cannot wet the solute particles, they separate more readily (attributed to mostly buoyancy of trapped

air), and slurry viscosity measurement may be challenging. *Therefore, the wettability of adsorbents is critical for slurry making and must be characterized and differentiated from adsorption for adsorbent powders.*

More intriguing hypotheses can be made about these phenomena. Before the accumulation of any solvent on their surface, adsorbent particles have high free surface energy as compared to the surface tension of the liquid [22]. This surplus surface energy should assist in excellent wetting of the particles, favoring adsorption. Once the solvent molecules begin to adsorb, this surface energy decreases, rendering the subsequent wetting difficult as the surface tension of liquid solvent may exceed the surface energy of the adsorbents. Therefore, there must be a correlation between the amount of solvent in contact with the particles after adsorption and the contact angle after this adsorption (describing wetting or lack of wetting). Because this adsorbed liquid has already become immobile with respect to particles, its role in defining the mixture viscosity is restricted. This affects the slurry viscosity in two ways. First, the interactions between immobilized and free liquid differ from those between particles and free liquid. This change can be determined using zeta potential (ζ), the electrokinetic potential at the interface between adsorbed and free liquid. Higher ζ means stable slurry through particulate repulsion, whereas smaller ζ makes particles flocculate, causing eventual separation. For example, the ζ for water-MIL-101 (Cr) is -2.7 mV [24], whereas the same for silica slurry is -40 mV [25]. It means silica slurries are more stable because of repulsive forces between particles; however, MIL-101 (Cr) will tend to flocculate and sediment out of the slurry. Second, because of solvent adsorption, the free liquid fraction in the total slurry is reduced, indirectly affecting the solid volume fraction of the slurry.

Therefore, measuring contact angle as a function of wetting carries tremendous importance. It could be hypothesized that the initial contact angle between the adsorbent and solvent is very low, resulting in excellent wetting until adsorption takes place after that, increasing to an equilibrium value because of a drop in surface energy. While the measurement of contact angle is beyond the scope of this thesis, it is given necessary treatment in the theoretical framework.

Due to the lack of convincing experimental results or models, a set of powders and solvents with differentiable properties was selected, shown in Table 1. MIL-101 (Cr) (procured from NanoChemaZone) was chosen as the adsorbent, as it shows excellent water and ethanol adsorption capacities (1.26 kg kg^{-1} and 0.92 kg $kg^{-1,}$ respectively, for a specific surface area (SSA) of 2936 m^2 g^{-1} [26]). The SSA (also known as BET area) measured for the MIL-101 (Cr) procured for this experiment was measured at Florida Tech to be 1562 m^2 g^{-1} and resulted in a water uptake capacity of 0.52 kg kg^{-1} [27]. Note that the desorption of these solvents in high amounts during the drying stage of the washcoating process and forming macropores is crucial for the discussions in Chapter 3.

SiO_2 and TiO_2 (SkySprings Nanomaterials, Inc) have always been used as binders for adsorbent structuring [28]. They have a unique combination of tiny size (5 nm – 20 nm) and porous surface with non-zero SSA; therefore, they represent nanometer-scale adsorbents for this study. Uniform glass spheres or beads (Mo-Sci) have been used for experimental validation of theoretical models, providing a basis for comparing adsorbent and non-adsorbent powders. The glass beads used in these tests are spherical (confirmed via SEM), SiO_2 and TiO_2 are mostly spherical [29, 30], while MIL-101 (Cr) particles are 3D hexagonal

shaped (confirmed via SEM). None of the materials in Table 1 have elongated chain-type or fibrous shape that has been thought to influence viscosity [31]. Meanwhile, water is the universal solvent for all purposes, and ethanol was chosen for its excellent wetting ability over water [32].

Table 1. Materials and Solvents used for the preliminary study on the viscosity of adsorbent slurries.

Solid Powders					
Material	**Powder Density [kg m^{-3}]**	**True Density [kg m^{-3}]**	**Average Particle size**	**BET Area [m^2 g^{-1}]**	**Porous?**
MIL-101 (Cr) [27]	600 (Measured)	2000 (Assumed)	1 μm	1562 (measured)	Yes
SiO_2 [30]	100	2648	15 nm	640	Yes
TiO_2 [29]	700 (Measured)	4230	5 nm	250	Yes
Glass Beads [33]	1300	2500	10 μm	0	No
Solvents					
	Base Viscosity		**Contact angle on quartz [32]**		
Distilled Water	1 mPa-s (measured)		30°		
Pure Ethanol	1.25 mPa-s (measured)		0°		

2.3 Test Procedure

The experiment is commenced by first investigating the US Solid USS-DVT6 viscometer accuracy. This is performed by determining the viscosity of silicone oil for different Revolutions Per Minute (RPM) to validate its Newtonian fluid behavior and compare the measured values with the reported data. The test ensured the consistency of the readings, as shown in **Figure 2**, which depicts the Newtonian behavior as anticipated, thereby eliminating the potential for discrepancies that could render the actual experimental results invalid.

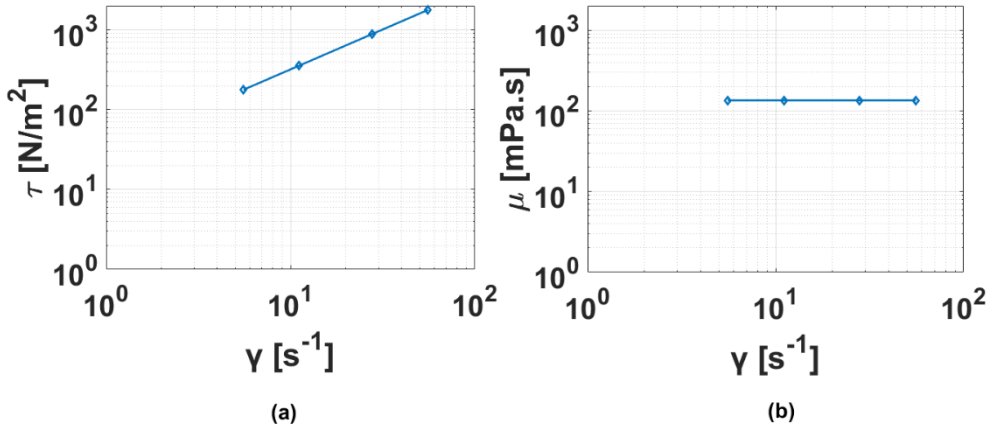

Figure 2: Silicone oil (a) shear stress (b) viscosity at varied strain rates

The slurry viscosity experiments are divided into two sets depending on the type of solvent used. The first set utilizes distilled water (procured from Snugell) as the primary solvent with a base viscosity of 1 mPa-s. The second set employs anhydrous ethyl alcohol or ethanol (Pharmaco) as the base solvent with an initial viscosity of 1.25 mPa-s. Solutes of varied sizes and properties are then added to the individual solvent to determine the rheological properties of the slurry.

2.3.1 Tests for Solutes in Distilled Water

The solutes in Table 1 behave differently due to their size, shape, and adsorption properties when introduced into distilled water. For each experiment, 25 ml of distilled water is used as a base solvent, poured into a clean steel container of diameter 13.8 mm and height 135 mm. A weighing boat provided by Avogadro's Lab Supply is used to measure the weight of the solute, which is then added to the distilled water. The initial mass for all solutes is 0.25

g, corresponding to a 1% mass fraction, except for silica nanoparticles which begin at 0.1 g. Since the bulk density of silica nanoparticles is the smallest, they have a more significant number of particles, resulting in a significantly high volume fraction. A glass stirrer is then used to distribute the monodisperse solute within the solvent over 60 seconds to ensure adequate mixing and prevent the solute from settling at the bottom due to density variations between the solutes and solvents. Subsequent experiments showed that increasing the mixing time did not significantly affect viscosity values. The steel vessel containing the slurry is then suspended onto the viscometer, where a rotor of diameter 12.4 mm is used to determine the slurry viscosity. These measurements are obtained at 6, 12, 30, and 60 RPM speeds. After measuring the viscosity values for a given volume fraction, an additional 0.25 grams of solute is introduced into the slurry, and viscosity values are recorded at different strain rates. The incremental value is kept at 0.1 grams for the silica slurry experiment.

2.3.2 Tests for Solutes in Ethanol

The methodology of the experiment mirrors that of distilled water experiment. To ensure an uncontaminated environment, the steel container and the rotor are meticulously cleaned with ethyl alcohol. This step is crucial as it eliminates foreign particles or remaining water molecules. Afterward, 25 ml of ethyl alcohol is poured into the container to begin the experiment. The remainder of the experiment follows the identical procedure outlined for the distilled water base experiment.

2.3.3 Adsorbent Slurries for Washcoating Applications

The experimental procedure for the slurry mixture of colloidal silica nanoparticles and suspension of MIL-101 (Cr) is slightly different from the individual solute-based slurry experiments. The experiment begins by weighing MIL-101 (Cr) at 0.25 g in a weigh boat, which is then introduced into the steel vessel containing 25 ml of either water or ethyl alcohol. This is followed by adding 0.1 grams of silica nanoparticles into the slurry containing MIL-101 (Cr) and the solvent, which is then stirred for uniformity. After stirring, the steel container is suspended onto the viscometer, where the rotor records viscosity values similar to other experiments. Once the values have been recorded at a certain volume fraction, more silica is incrementally added, each time by 0.1 grams, to derive new viscosity values until the total added mass of silica matches that of the MIL-101 (Cr) after which additional MIL-101 (Cr) is added to the slurry and the process continues. A pivotal step in this experiment is ensuring that the starting MIL-101 (Cr) volume fraction surpasses that of the silica fraction, which helps analyze the impact of silica nanoparticles on slurries with large particles of MIL-101 (Cr).

2.4 Results and Discussion

2.4.1 Silica Nanoparticle Slurry

When silica nanoparticles are added to distilled water, the slurry viscosity increases due to the solid particles interacting with the polar molecules of water. As more particles are introduced, a steady, non-linear rise in the viscosity of the slurry is observed, as shown in Figure 3 (a). It is observed that the shear stress and strain rate are not proportional, which is

also confirmed by the viscosity vs. strain rate plot in Figure 3 (b), indicating shear thinning non-Newtonian behavior. This behavior is driven by the adjustment in particle orientation in response to an increase in strain rate. At higher strain rates, the particles can no longer maintain their temporary bonds and will instead flow in the direction of the fluid motion induced by the rotor.

At low volume fraction, the colloid concentration within the slurry is considerably smaller than water, resulting in the particles having a large mean free path, which suggests that the particles are not subject to aggregation and can remain freely suspended. With increased silica volume fraction, the shear stress curves show an upward shift, implying an increase in viscosity, maintaining shear thinning properties. This is complemented by the zeta potential (ζ) theory that high values of electrokinetic potential result in a stable slurry [25]. As the concentration of particles or volume fraction increases, the cohesive forces among water molecules diminish, further augmenting the shear thinning behavior.

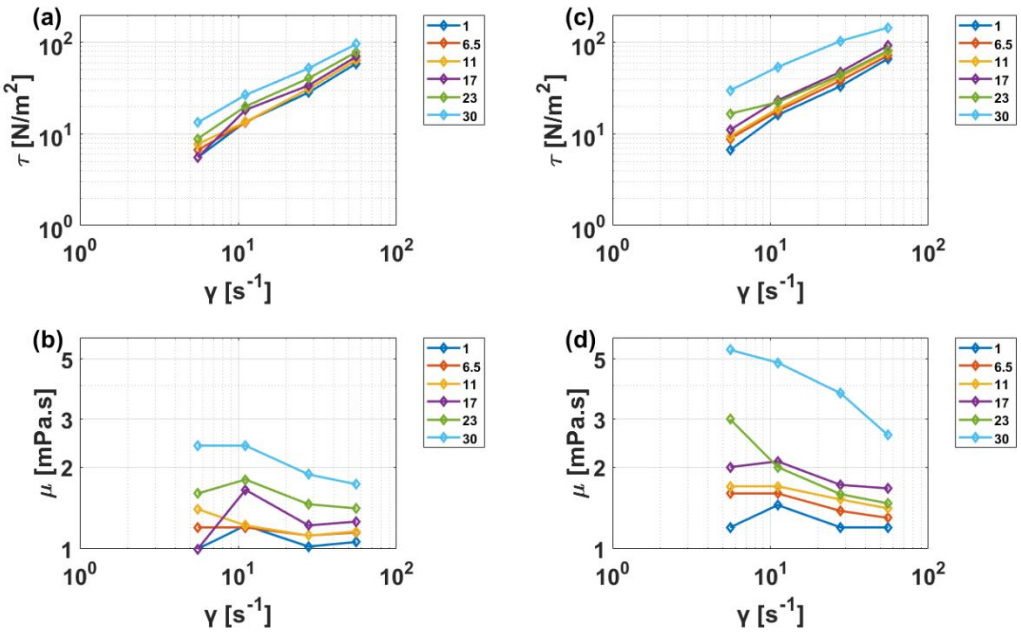

Figure 3: (a) Shear stress vs strain rate for SiO_2 in water. (b) Viscosity vs. Strain rater for SiO_2 in water. (c) Shear stress vs. strain rate for SiO_2 in ethanol. (d) Viscosity vs. strain rate for SiO_2 in ethanol

The increase in the viscosity is gradual till a volume fraction of 36%, after which there is a moderate change in the viscosity due to the formation of aggregates**.** Beyond the 46% volume fraction, a sharp rise in viscosity is observed, marking the beginning of what can be termed the 'high viscous stage' (Not shown in Figure 3)

Figure 3(c) shows that adding silica nanoparticles in ethyl alcohol results in higher viscosity when compared to distilled water. The baseline solvent viscosity is higher for ethanol than water, and wetting (contact angle for water and ethanol) could be attributed to this change. Figure 3(d) shows the shear thinning behavior of silica nanoparticles and becomes more

apparent at higher volume fractions. Similar to the DI water experiment, the slurry thickens at higher volume fractions, necessitating continuous stirring as the particles have the potential to form a thread-like network where the viscosity increases exponentially. It can be hypothesized that ethanol allows better wetting than water, therefore, more surface coverage, which results in more water entering the particles, resulting in a more dramatic effect of viscosity.

2.4.2 TiO_2 Slurry

Adding 5 nm anatase Titania particles into DI water exhibits shear thinning behavior, as shown in Figure 4((a) and (b)). Similar to the behavior of silica nanoparticles in DI water, the shear stress and strain rate values are not proportional. This non-proportionality increases with the volume fraction, and the plotted curve indicates that the particles are well dispersed at higher strain rates. This dispersion is also a consequence of the small size of the particles, further contributing to a slow rise in viscosity as the volume fraction increases. Initially, water primarily governs the rheology of the slurry, but when the solute concentration increases, the dependency falls on the solutes. However, aggregates are formed due to interparticle forces between solute and solvent at high volume fractions but can be eliminated by stirring the solution. Another critical factor to consider for the viscosity is the contact angle between water and titania particles. This enables particle wetting but does not substantially impact the viscosity of water-based solvents.

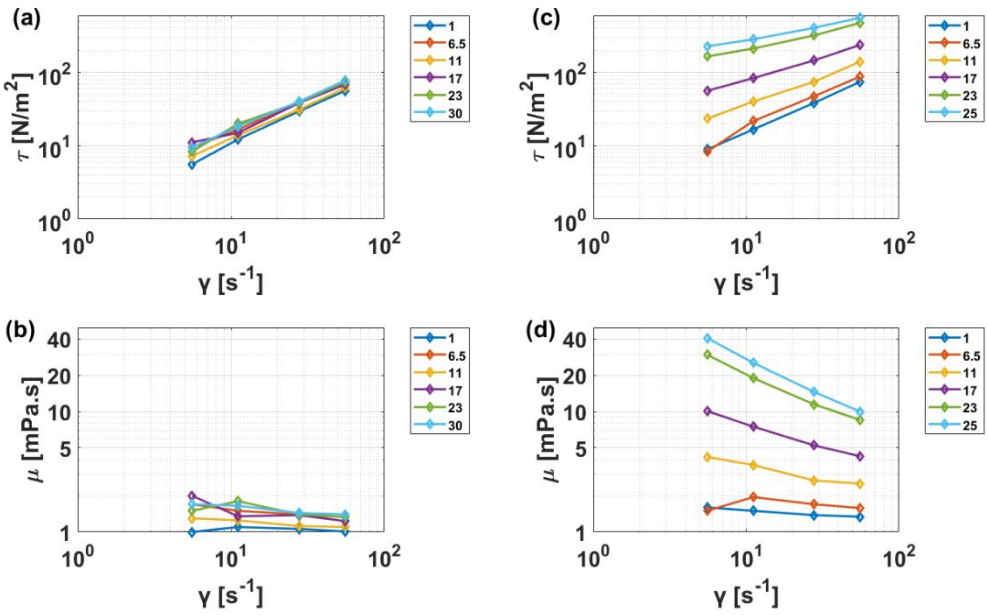

Figure 4: (a) Shear stress vs strain rate for TiO_2 in water. (b) Viscosity vs. Strain rater for TiO_2 in water. (c) Shear stress vs. strain rate for TiO_2 in ethanol. (d) Viscosity vs. strain rate for TiO_2 in ethanol

A significant effect observed in the mix of titania and water is a color shift, likely due to the Tyndall effect [34]. The transformation led to a blueish slurry from its initial white appearance, possibly due to the optical properties of the mixture absorbing blue light from the visible light spectrum. Although Titania is known for absorbing the visible spectrum and having practical applications, it's worth noting that the small particle size could also induce color changes but is not validated in this experiment (Note that the color of silica nanoparticles did not exhibit any changes), as shown in Figure 5. Furthermore, removing the oxide layer on TiO_2, potentially due to hydrogen molecules interacting with oxygen and, thus, exposing titanium to water, changes its color. Another significant factor contributing to color change is water adsorption onto TiO_2 Particles [35]. As shown in Table 1, the TiO_2

nanoparticles have a non-zero SSA. However, this effect must be quantified further to corroborate these hypotheses.

When TiO_2 is added to ethanol, the viscosity experiences a more significant increase due to the interaction between the particles and the solvent, which happens to be similar to the SiO_2 slurry. The color transformation for TiO_2 slurry with ethanol isn't instantaneous but occurs slowly over time as aging initiates, allowing light penetration into the ethyl alcohol. As the concentration of TiO_2 intensifies, so does the degree of flocculation. However, stirring can mitigate this, enabling more effective particle dispersion.

Figure 5: TiO_2 (left) light blue color & SiO_2(right) white color

2.4.3 MIL-101 (Cr) Slurry

Adding MIL-101 (Cr) into distilled water indicates a marginal increase in viscosity at low-volume fractions. The rise in the slurry viscosity proceeds in a gradual trend as more MIL-101 (Cr) particles are introduced into the slurry, as shown in Figure 6(a). This steady progression remains stable even at higher volume fractions compared to nanoparticle slurry

behavior, where they exhibit an exponential increase in viscosity. Shear thinning behavior is also observed for MIL-101 (Cr) slurry and is pronounced at high volume fractions, as shown in Figure 6(b). The hexagonal shape of MIL-101 (Cr) does not form chain-like structures with other particles, even at high-volume fractions. Instead, due to the presence of edges in the particle shape, it tends to displace other particles preventing network formation and allowing the particle to align themselves with fluid motions at different strain rates. Some agglomeration is observed at high volume fractions due to the polar attraction of the solid molecules (note that the ζ potential for MIL-101 (Cr) water slurry is small, indicating unstable slurry prone to flocculation).

Shear thinning behavior is seen more prominently with MIL-101 (Cr) slurry in ethanol, as shown in Figure 6 (c) and (d), which can be attributed to the adsorption of ethanol coupled with excellent wetting. Therefore, the effect on viscosity, in general, is more prominent than water. Additionally, as the concentration of MIL-101 (Cr) increases, more ethanol is adsorbed into the pores of the particles as more new sites are available.

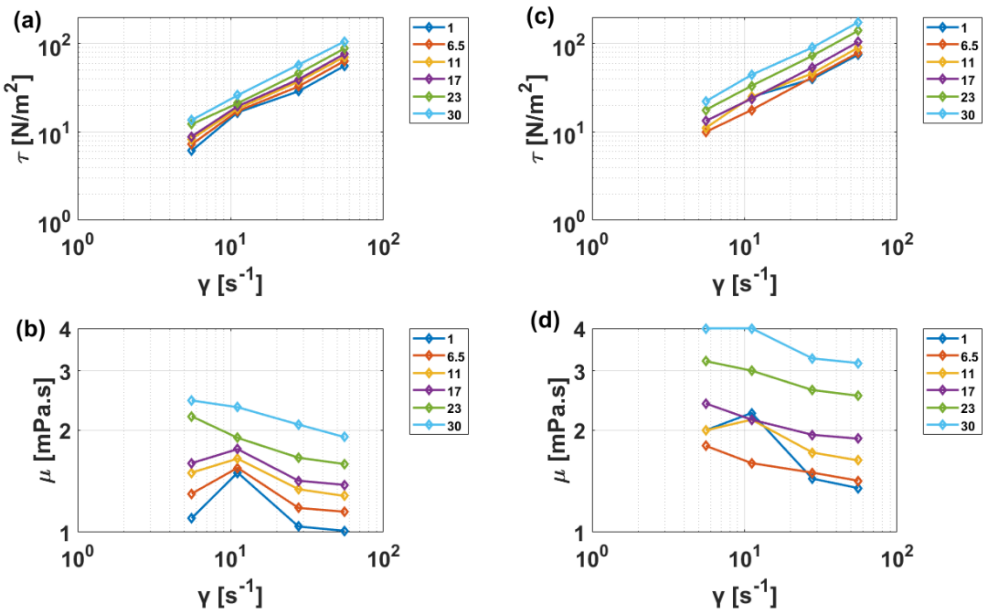

Figure 6. (a) Shear stress vs. strain rate for MIL-101 (Cr) in water. (b) Viscosity vs. Strain rater for MIL-101 (Cr) in water. (c) Shear stress vs. strain rate for MIL-101 (Cr) in ethanol. (d) Viscosity vs. strain rate for MIL-101 (Cr) in ethanol

2.4.4 Glass Bead Slurry

Glass bead slurries show interesting patterns despite being non-porous. Adding these beads to distilled water only causes a minor and linear increase in viscosity at low volume fractions. This is because glass beads align based on the strain rate within distilled water and are more dispersed**.** Figure 7(a) shows the pattern remains the same even at elevated concentrations with a volume fraction of 50%, where the shear stress values experience a gradual increase and shifts upwards.

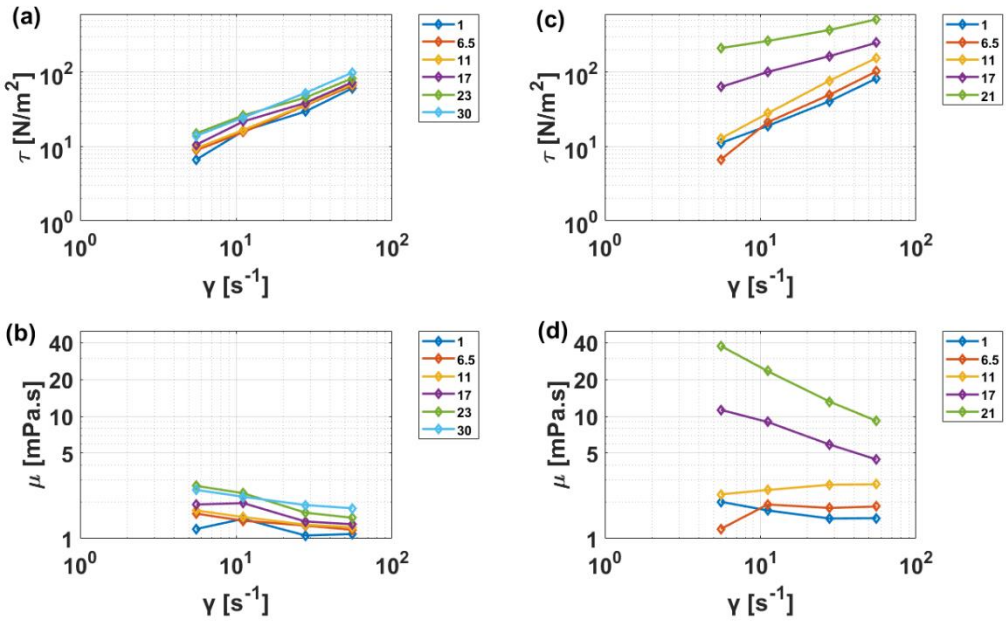

Figure 7. (a) Shear stress vs. strain rate for glass beads in water. (b) Viscosity vs. Strain rater for glass beads in water. (d) Shear stress vs. strain rate for glass beads in ethanol. (d) Viscosity vs. strain rate for glass beads in ethanol

The spherical shape of these beads averts the formation of chains and highlights the role of water molecules as the primary intermolecular forces in the mix. The absence of pores also influences aggregation, with small clusters forming only when the slurry is undisturbed at volume fractions above 30%. Since the bead density surpasses that of water, they tend to sediment more readily, making stirring a prerequisite for mixture homogeneity.

Figure 7(b) highlights the shear thinning behavior for glass beads slurry. Additionally, since the glass bead particles are larger than substances like silica and TiO_2, it can be inferred that size plays a substantial role due to a smaller particle count for the same volume fraction. Even though their spherical nature should limit alignment variations, increased concentration

leads to more collisions between the particles. The contact angle of distilled water is another significant factor in viscosity determination. Since glass particles do not have pores, the adhesion of water molecules depends on the wetting of the glass particles alone. Increasing the volume fraction reduces the contact angle, permitting more wetting but not enough to cause a dramatic increase in viscosity for the glass beads.

Glass beads slurry in ethanol shows the most dramatic change in viscosity, as shown in Figure 7(c), which can be hypothesized to be controlled by wetting alone. Adsorption, or solvent entry into the pores of the particles in the case of glass beads, is impossible. Therefore, the change of solvent can only affect the wetting characteristics. Ethanol has already been measured to have a 0° contact angle with glass, which becomes instrumental in this mixture [32]. The shear thinning behavior is observed in the early stage of the experiment but gets more prominent beginning from the 10% volume fraction, as shown in Figure 7(d) and thereby can be divided into two distinct stages. The first stage is characterized by a steady increment in the number of particles, whereas the subsequent stage sees an upsurge in particle wetting due to the zero contact angle of ethyl alcohol. This improved wetting leads to a significant surge in viscosity.

The adhesive forces, in effect, arise from the fact that molecules, regardless of their shape or size, display increased dispersion as wetting intensifies. After that, sedimentation occurs not only at the base because of the higher true density of the glass beads but also at the top of the rotor because of increased adhesive forces between the rotor's top surface and the solid particles immersed in ethyl alcohol; this explains that the particles will gravitate towards the nearest surface.

2.4.5 Washcoating Slurry (MIL-101 (Cr) + SiO_2 + Solvent)

When MIL-101 (Cr) and silica nanoparticles are simultaneously introduced into distilled water or ethyl alcohol, the fluid resistance notably increases, consequently raising the viscosity. This increase is visible even at the possible minimal strain rate and the smallest volume fraction for the experiments conducted, an observation not encountered when the solutes were added individually in the solvents. This pattern implies that polydispersity contributes to these heightened values since the shape and size differ significantly.

MIL-101 (Cr) hexagonal shape and the tendency of silica particles to bind with solvent and other particles can dictate the adherence of silica nanoparticles to MIL-101 (Cr) particles. This hexagonal configuration allows silica particles to organize themselves first along the edges and subsequently on the faces, thereby amplifying the shear in the slurry. This configuration can induce a change in the particle's shape to a certain extent. In the case of ethyl alcohol, as seen in the individual solute experiments, the values are more accentuated due to a decrease in the contact angle. The emergence of new shapes also enlarges the surface area, potentially affecting wettability, although the contact angle depends on the shape. From Figure 8, it can also be deduced that the inclusion of MIL-101 (Cr) results in a considerable increase in viscosity. This observation suggests that the larger size facilitates a higher viscosity as the silica particles adhere or bind to the MIL-101 (Cr) particles. This increased viscosity is vital in the washcoating process described in the next chapter.

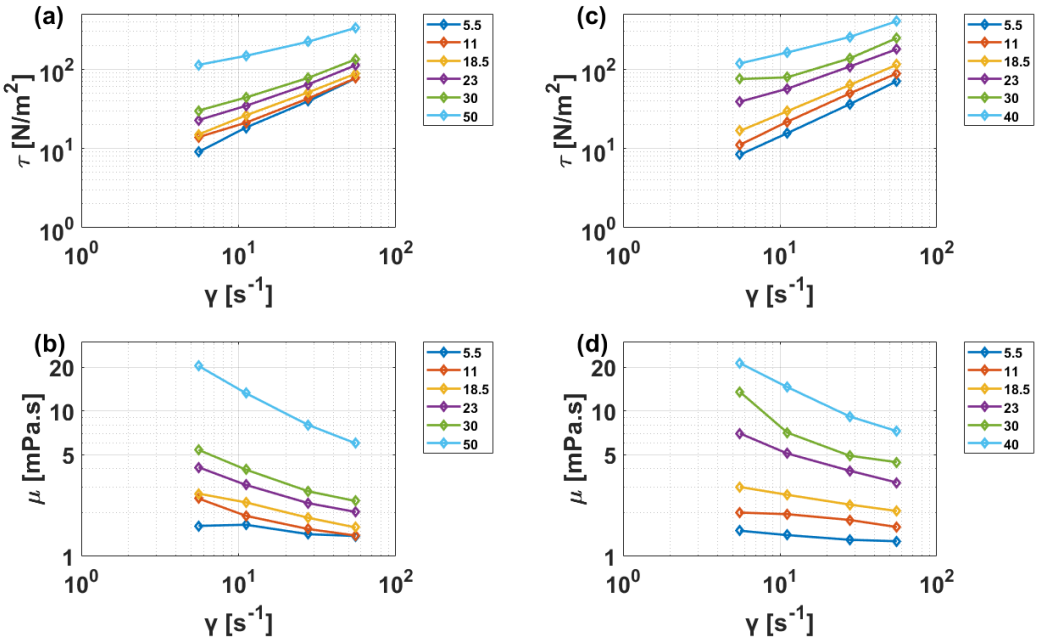

Figure 8. (a) Shear stress vs. strain rate for mixture in water. (b) Viscosity vs. Strain rater for mixture in water. (c) Shear stress vs. strain rate for mixture in ethanol. (d) Viscosity vs. strain rate for mixture in ethanol

2.4.6 Comparative Assessment

Upon comparing solutes in water-based solvents, it is observed that at very low volume fractions, the shear stress values for MIL-101 (Cr) are less than those for other solutes for given strain rates. This pattern can be linked to the larger available size and fewer MIL-101 (Cr) particles relative to the other solutes. As the volume fraction rises, there's a significant increase in MIL-101 (Cr) shear stress values, as depicted in Figure 9(a) and (b), followed by glass beads, silica nanoparticles, and titania. However, a contrasting pattern emerges when these solutes are mixed with ethanol, shown in Figure 9(c) and (d). At low volume fraction

MIL-101 (Cr) exhibits high shear stress values at a given strain rate, but as the volume fraction increases, shear stress values of glass beads exceed those of MIL-101 (Cr) by around 10% volume fraction. The trend of shear stress values proceeds as glass beads, titania, MIL-101 (Cr), and silica nanoparticles. It's worth highlighting that the shear stress values of even the titania nanoparticles exceed those of MIL-101 (Cr), implying that the behavior of slurries can vary depending on the solvent used.

On comparing the behavior of nanoparticle colloids in water, it is observed that titania particles, smaller than silica nanoparticles, represent higher resistance to the fluid at a lower volume fraction. However, as the volume fraction increases, silica nanoparticle resistance increases. This signifies that the number of particles initially governs the viscosity. However, resistance starts to rely more on other attributes as the volume fraction increases. Unlike in water, the titania slurry with ethanol shows higher viscosity than silica nanoparticles, irrespective of the volume fraction. This distinct trend significantly alters the observation from the water-based experiments, indicating that particle size, while an important factor, cannot determine the viscosity completely.

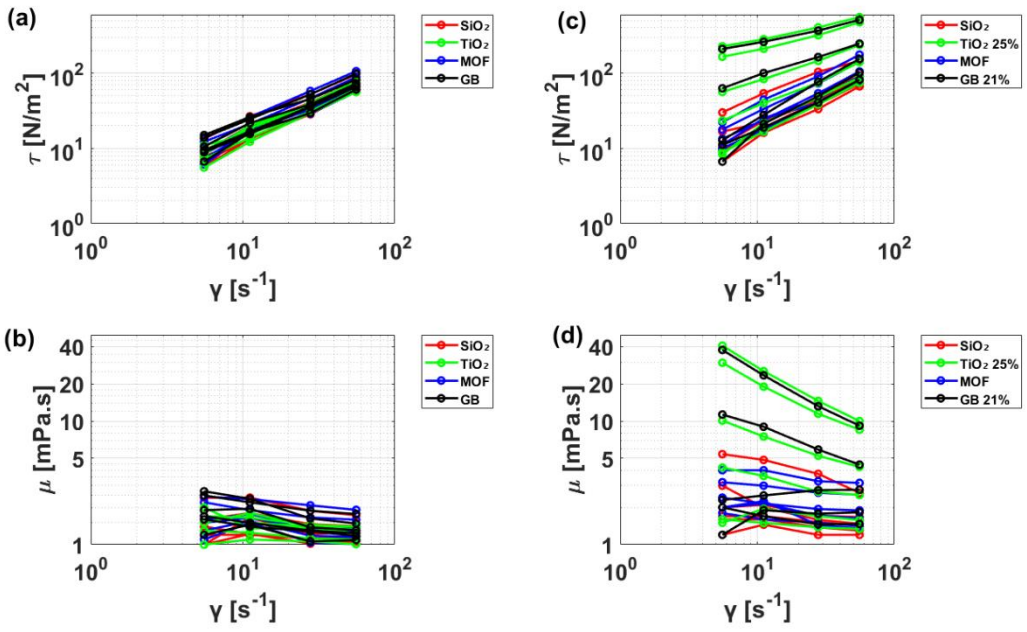

Figure 9. (a) Shear stress vs strain rate for all water-based slurry. (b) Viscosity vs. Strain rater for all water-based slurry. (c) Shear stress vs. strain rate for all ethanol-based slurry. (d) Viscosity vs. strain rate for all ethanol-based slurry

It is clear that solvent adsorption onto porous adsorbent particles significantly impacts the viscosity, complemented by wetting by solvents to varied degrees. An increase in adsorption capacity corresponds with a gradual and steady increase in slurry viscosity, as observed for MIL-101 (Cr) in both solvents. Conversely, the viscosity of glass beads in ethanol rises more rapidly with volume fraction due to enhanced particle wetting, indicating that smoother surfaces might be more susceptible to wetting. However, the viscosity increase in water is neither rapid nor significant, emphasizing the contact angle and wetting capability as the primary factors. Compared to water, the pattern of increased viscosity in ethanol is also evident in the case of silica and titania nanoparticles.

Moreover, titania slurries show higher viscosities in ethanol and surpass silica colloid viscosity, which is an antithesis to adsorption increasing viscosity. However, better wetting on a less porous surface should result in higher viscosity, which supersedes any effect that adsorption might have had on the slurry viscosity.

These tests show that adsorbent slurry viscosity is a complex property that depends on multiple factors, which may be intimately coupled with each other. Therefore, a measurement-driven and physics-based approach is needed to establish the connection between the independent variables and the slurry viscosity.

2.4.7 Semi-Empirical Model

The Buckingham Π theorem defines dimensionless parameters and Π terms to establish a semi-empirical model for the slurry viscosity. This entails identifying and expressing the parameters of fundamental quantities such as Mass, Length, and Time (M L T) relevant to the experiments. Subsequently, these fundamental quantities will be applied to a recurring set of geometric, flow, and fluid properties, from which a repeating set of variables and Π terms will be derived. To set the parameters, first, the variables that directly influence the viscosity of the slurry are determined, which are shown in Table 2.

Table 2: Parameters defined for the model

	Parameters	Experimental Units (SI)	Simplified Units	Fundamental Dimensions
1	μ_{slurry}	mPa.s	kg/(ms)	$M^1 L^{-1} T^{-1}$
2	μ_{base}	mPa.s	kg/(ms)	$M^1 L^{-1} T^{-1}$
3	ρ	g/cm^3	kg/m^3	$M^1 L^{-3}$
4	D	nm or µm	m (meter)	L^1
5	γ	1/s	1/s	T^1
6	φ	Dimensionless	ml/ml	---
7	$\bar{N}$	Dimensionless	-	---
8	α	Degrees	-	---

μ_{slurry} indicates the overall viscosity when the solute is added to the solvent. $\mu_{solvent}$ represents the base solvent, which, in the context of the slurry, is now autonomous, thereby allowing the use of any base solvent. Density is defined by ρ, which is the true density to account for the inherent physical property of the particles. D as the diameter of the particles, given the crucial role that size plays in viscosity determination. The shear rate is defined by γ which will dictate Newtonian or non-Newtonian behavior of the slurry. The modified volume fraction is defined by φ, as shown in Eq.(3) , where θ is the actual volume fraction and C_A is the adsorption capacity of the solute. $\bar{N}$ denotes the ratio of the number of water molecules to solute molecules, whether or not adsorption is present to the number of solute particles in the slurry, giving an insight into viscous behavior, and α accounts for the actual wetting and its consequent impact on slurry viscosity.

A few parameters are not considered in this model. They are the slurry temperature, correction for the shape of the molecules and zeta potential (ζ). All the tests are conducted at the same temperature of 22°C, whereas the shape of the particles considered in this study is primarily spherical or symmetric, without any threadlike variations. Relative temperature can be considered in this study to generate another Π term, which is critical; however, the experiments would be beyond the scope of this thesis. Also, the role of ζ in directly determining slurry viscosity is unclear, although it has been used to predict slurry stability and sedimentation through flocculation. On a macroscopic level, it is a significant measurable indicator of the inter particulate force; therefore, it must be discussed. It could be considered if a direct connection between ζ and μ_{mix} is found; however, at the risk of double counting the same phenomenon. Note that C_A and ζ are intimately coupled, as solvent adsorption on the free particle surface alters its charge directly, and C_A has already been considered in the model. For now, it is not shown in the current version of the model to avoid overfitting the data.

Eight dependent variables, as shown in Eq. (4), and three fundamental quantities (M L T) indicate the need for five Π terms. Sets of repeating variables are determined in light of their potential impact on the experiment and the properties. The following parameters are considered to establish fundamental quantities: the diameter is chosen to provide the geometric characteristic, which equates to the quantity [L^1]. The shear rate represents the flow characteristics and aligns with the time property [T^1]. Lastly, density is determined to fulfill the fluid property and provides [M^1 L^{-3}]. As such, Diameter (D), Shear Rate (ϒ), and

Density (ρ) together form the set of repeating variables. Subsequently, the six pi terms are characterized.

$$\varphi = \frac{1}{\frac{1}{\theta} - C_A} \tag{3}$$

$$\mu_{slurry} = f(\mu_{solvent}, \rho, D, \gamma, \varphi, \bar{N}, \alpha) \tag{4}$$

The primary pi term Π_1 Eq. (5) which is positioned on the function's left side, indicates that the slurry's viscosity is divided by the square of the particle's diameter, the strain rate at which the slurry is subjected to in the experiments, and the density of the particle. This ensures that individual particles' fundamental effects and properties are incorporated to understand the resistance within the slurry affecting the viscosity.

1. $\Pi_1 = D^{a1}\gamma^{b1}\rho^{c1}\mu_{slurry}$

$$L^{a1}\left(T^{-1}\right)^{b1}\left(M^1L^{-3}\right)^{c1} \quad M^1L^{-1}T^{-1} = M^0L^0T^0$$

Solving above

$$a_1 = -2;\ b_1 = -1;\ c_1 = -1$$

$$\Pi_1 = D^{-2}\Upsilon^{-1}\rho^{-1}\mu_{slurry}$$

$$\Pi_1 = \frac{\mu_{slurry}}{D^2\gamma\rho} \tag{5}$$

The second pi (Π_2) term Eq.(6) presents the base solvent divided by the same variables mentioned in the first pi term. This assists in gaining insight into how the solute reacts to the solvent viscosity.

2. $\Pi_2 = D^{a2}\gamma^{b2}\rho^{c2}\mu_{base}$

$$L^{a2}\left(T^{-1}\right)^{b2}\left(M^1L^{-3}\right)^{c2} \quad M^1L^{-1}T^{-1} = M^0L^0T^0$$

Solving above

$$a_2 = -2;\ b_2 = -1;\ c_2 = -1$$

$$\Pi_2 = D^{-2}\Upsilon^{-1}\rho^{-1}\mu_{base}$$

$$\Pi_2 = \frac{\mu_{base}}{D^2\gamma\rho} \tag{6}$$

The remaining pi terms Π_3, Π_4, and Π_5 are inherently dimensionless. When multiplied by the repeating variables, these terms yield the same variables previously defined.

3. $\Pi_3 = D^{a3}\Upsilon^{b3}\rho^{c3}N$

$$L^{a3}\left(T^{-1}\right)^{b3}\left(M^1L^{-3}\right)^{c3} \quad M^0L^0T^0 = M^0L^0T^0$$

$$\Pi_3 = \bar{N} \tag{7}$$

4. $\Pi_4 = D^{a4}\Upsilon^{b4}\rho^{c4}\theta$

$$L^{a4}\left(T^{-1}\right)^{b4}\left(M^1L^{-3}\right)^{c4} \quad M^0L^0T^0 = M^0L^0T^0$$

$$\Pi_4 = \varphi \tag{8}$$

5. $\Pi_5 = D^{a5}\Upsilon^{b5}\rho^{c5}\cos\alpha$

$$L^{a5}\left(T^{-1}\right)^{b5}\left(M^1L^{-3}\right)^{c5} \quad M^0L^0T^0 = M^0L^0T^0$$

$$\Pi_5 = \cos\alpha \tag{9}$$

After defining the pi terms, they are plotted to analyze and develop a semi-empirical model. First, Π_1 is plotted against Π_2 for all solutes in water. Evaluating these two Π terms will reveal the impact of variables like particle size, density, and strain rate on the slurry's relative viscosity and solute concentration and how these factors influence viscosity. Figure 10 implies an exponential relation between them. Furthermore, as the denominator is the same, the primary difference is the numerator which accounts for the calculated viscosity from the experiment at different strain rates, which depicts the shear thinning behavior. The addition of more solutes enhances this behavior, which aligns with the results from the experiment.

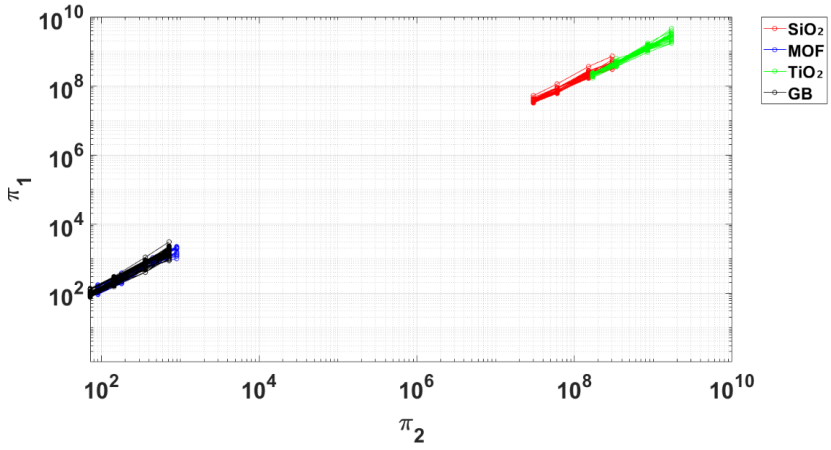

Figure 10: Π_1 plotted against Π_2 for all solutes

To accommodate the particle-to-particle concentration, Π_3, a ratio of the number of water molecules to the number of solute particles, is multiplied into the denominator of Π_1 and Π_2 terms. Figure 11 shows that the values of Π_1 and Π_2 decrease as the number of particles increases. Additionally, it is observed that the plotted lines start to collapse, indicating a

linear relationship between the variables. As the number of solute particles increased, the value of Π_3 declined for all the slurries. This decline is rapid in MIL-101 (Cr), silica, and titania due to the availability of pore sites where water molecules get incorporated, decreasing the ratio. The water volume remains constant in glass beads as no pore sites are available. Extended lines are observed as the ratio decreases; this is due to the influence of solvent on the overall viscosity as more solvent molecules dominate in the beginning. As the number of particles increases, this dependency changes to the number of solute particles, enhancing the viscosity and extending the plotted lines.

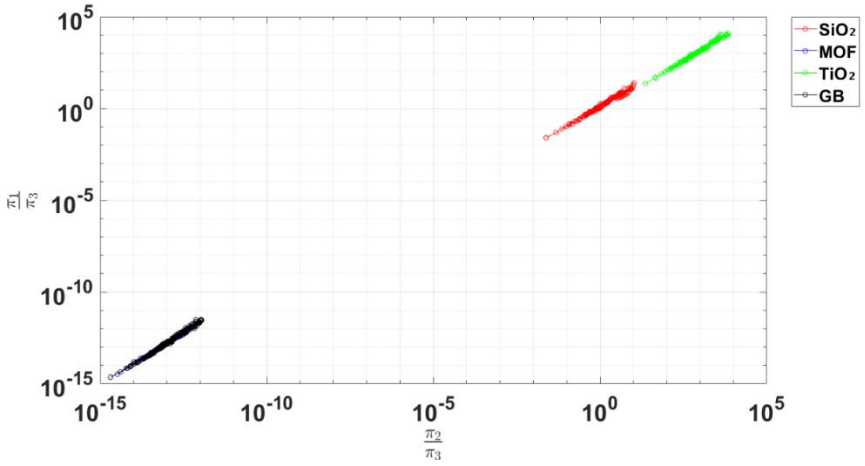

Figure 11: Linear effect of Π_3 on the model

An increased solute concentration corresponds to a larger volume fraction, which further influences the effective viscosity of the slurry. As a result, the adjusted Π terms are now divided by Π_4, i.e., the modified volume fraction. Figure 12 shows the effect of Π_4, which shifts the plotted lines leading to the non-collapsing plot**.** This is because the volume fraction incorporates the physical space that the particles occupy. In addition, it also accounts for the

adsorption capacity at every incremental solute concentration, further emphasizing the actual data sets.

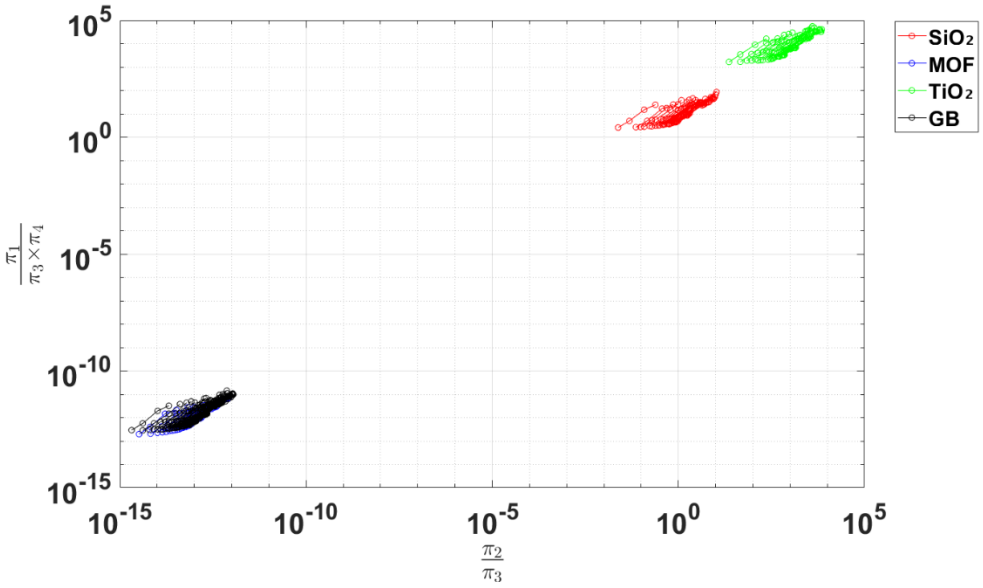

Figure 12: Divergence effect with the addition of Π_4 on the model

`

When comparing the different solutes, it is apparent that the line shifts for porous materials are more substantial due to the high adsorption of water molecules, as seen for MIL-101 (Cr) and glass beads in Figure 12. It can be stated that GB's characteristics are heavily influenced by wetting and the solvent's contact angle. This is the same reason that the viscous behavior for all slurries, irrespective of the solute, is more pronounced in ethanol.

The final pi term, Π_5, the wetting angle, is not yet considered in the model, but subsequent use of it has shown promising results. Overall, the plot suggests a linear dependence of the variables. Since the Π terms have established an exponential relation, the next step is to

evaluate the exponents of these terms. For this, all the Π terms of all the solutes that were plotted are used. Then the exponents are to be found and optimized such that all the lines collapse to make a straight line.

The derived pi terms' exponents are optimized using the NSGA II multi-objective algorithm to identify an ideal Pareto set. The gamultiobj method, a variant of the NSGA II technique, is applied to discover optimal solutions attained by passing the objective function to gamultiobj. Gamultiobj subsequently searches for the best values of the exponents (ex1, ex2, ex3, ex4) that minimize the output of the objective function. Another feature of this approach is the implementation of elitism, guaranteeing that superior solutions are transitioned to the following generation [36].

The plotted lines must be linear to enable the model to predict viscosity, which is achieved by employing the function pdist2 in the objective function. The pdist2 function calculates Euclidean distance, creating a straight-line path between two points within Euclidean space. Following optimization, the obtained values and all the data points fall on a straight line, as shown in Figure 13, with the exponent values equating to [0.1 0.1195 1 0.1]. Subsequently, all the data was manipulated to form a singular line for the entire dataset. This was accomplished using a loop and fitting variables in MATLAB, resulting in a straight line in Figure 14.

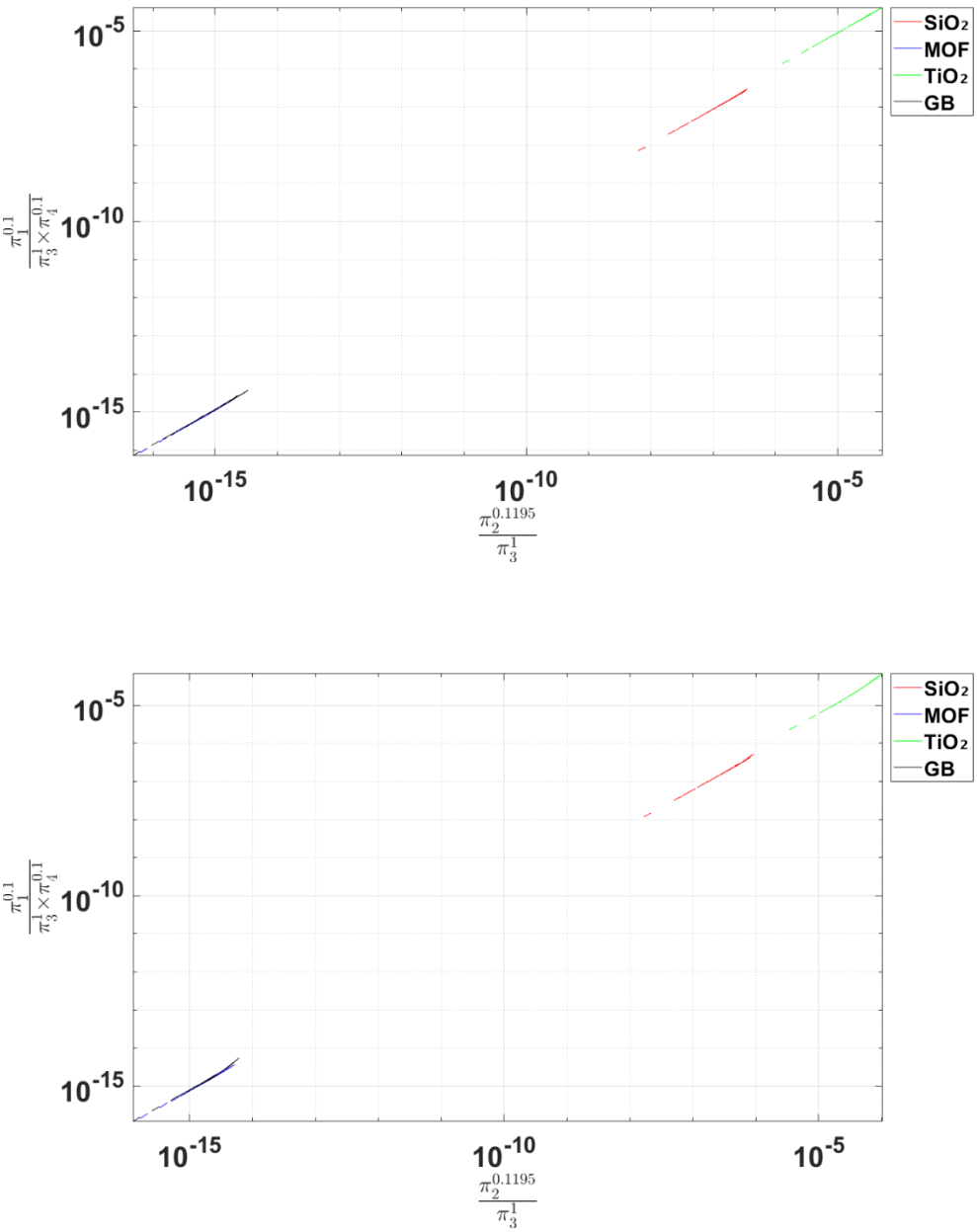

Figure 13: Collapse of the data points after optimization for (a) water slurry (b) ethanol slurry

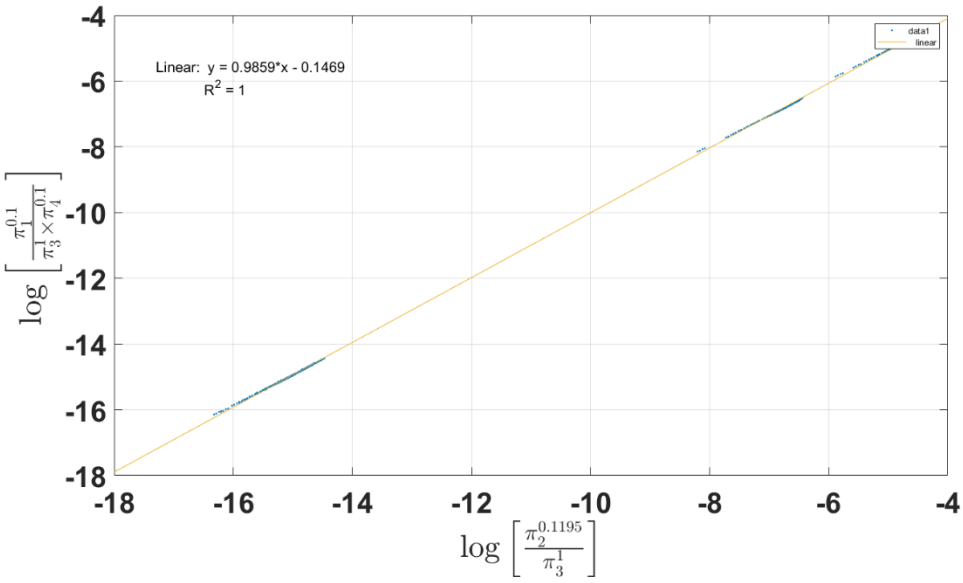

Figure 14: Linear fit for all the collapsed data.

The optimized exponent for Π_3 is determined to be 1, suggesting a pre-existing linear dependence that aligns with earlier observations. The optimized model, shown in Eq. (10) and (11), excludes contact angle since the experiments to determine the wetting were not conducted. However, as wetting plays a significant role in determining viscosity, after evaluating the model with the linear fit Eq. (12), the contact angle was introduced manually to ensure the consistency of the model.

$$\log\left[\frac{\pi_1^{0.1}}{\pi_3^{1}\pi_4^{0.1}}\right] = \log\left[\frac{\pi_2^{0.1195}}{\pi_3^{1}}\right] \tag{10}$$

$$\log\left[\left(\frac{\mu_{slurry}}{D^2\rho\gamma}\right)^{0.1}\frac{1}{N^1}\frac{1}{\varphi^{0.1}}\right]=\log\left[\left(\frac{\mu_{solvent}}{D^2\rho\gamma}\right)^{0.1195}\frac{1}{N^1}\right] \tag{11}$$

$$y=0.9859x-0.1469 \tag{12}$$

Equations (13) through (17) are obtained from the linear equation to the model using the antilog and exponent.

$$\log\left[\left(\frac{\mu_{slurry}}{D^2\rho\gamma}\right)^{0.1}\frac{1}{N^1}\frac{1}{\varphi^{0.1}}\right]=\log\left[\left(\frac{\mu_{solvent}}{D^2\rho\gamma}\right)^{0.1195}\frac{1}{N^1}\right]^{0.9859}-\log(1.402) \tag{13}$$

$$\frac{{\mu_{slurry}}^{0.1}}{D^{0.2}\rho^{0.1}\gamma^{0.1}N^1\varphi^{0.1}}=\left(\frac{{\mu_{base}}^{0.1195}}{D^{0.239}\rho^{0.1195}\gamma^{0.1195}N^1}\right)^{0.9859}\left(\frac{1}{1.402}\right) \tag{14}$$

$$\frac{{\mu_{slurry}}^{0.1}}{D^{0.2}\rho^{0.1}\gamma^{0.1}N^1\varphi^{0.1}}=\left(\frac{{\mu_{base}}^{0.1178}}{D^{0.2356}\rho^{0.1178}\gamma^{0.1178}N^{0.9859}}\right)\left(\frac{1}{1.402}\right) \tag{15}$$

$${\mu_{slurry}}^{0.1}=\left(\frac{{\mu_{base}}^{0.1178}N^{0.0141}\varphi^{0.1}}{D^{0.035}\rho^{0.0178}\gamma^{0.0178}}\right)\left(\frac{1}{1.402}\right) \tag{16}$$

$$\mu_{slurry}=\left(\frac{{\mu_{base}}^{1.178}N^{0.14}\varphi^{1}}{D^{0.35}\rho^{0.178}\gamma^{0.178}}\right)\left(\frac{1}{14.02}\right) \tag{17}$$

Equation (17) presents the model equation indicating that the slurry viscosity is proportional to the solvent's viscosity, water molecules' ratio to solute particles, and volume fraction, which entails the adsorption capacity. Additionally, the viscosity of the slurry is inversely proportional to the diameter of the particle, its density, and the strain rate. Model-wise, the strain rate can be considered an independent factor in future evaluation, depending on

parameters to identify the dilatant type behavior. The final equation (18) includes the contact angle, which should ideally be measured for each solute and solvent pair; however, it is considered constant for the two solvents used, yielding an excellent match.

$$\mu_{slurry} = \left(\frac{\mu_{base}^{1.178} N^{0.14} \phi^{1}}{D^{0.35} \rho^{0.178} \gamma^{0.178}} \right) \left(\frac{1}{14.02} \right) \left(\cos^2 \alpha \right) \tag{18}$$

Eq. (18) was tested at a 30% volume fraction to validate the model. Table 3 shows the model values against the experimental values. After factoring in a contact angle of 35° for water, the model's results closely matched the experimental data. Tests were conducted at a reduced volume fraction of 20% to substantiate the proposed hypothesis further. In this case, the contact angle was expected to rise, and indeed, at an angle of 39°, the model performed as anticipated.

Table 3: Model values against experimental values for 30% and 20% volume fractions for MIL-101 (Cr)

30%	**Strain rate**	**Experimental values**	**Model Values**	**Difference [%]**
	5.562286	2.45	2.82	15.19
	11.12457	2.34	2.49	6.61
	27.81143	2.08	2.12	1.89
	55.62286	1.91	1.87	-1.92

20%	**Strain rate**	**Experimental values**	**Model Values**	**Difference [%]**
	5.562286	2.1	2.40	14.49
	11.12457	1.9	2.13	11.86
	27.81143	1.48	1.81	21.99
	55.62286	1.51	1.60	5.69

Upon verifying the consistency of the model with the experimental data points, it was found that the results varied slightly due to not using the actual contact angles. Additionally, given that the contact angle was not experimentally determined and its exponent remains undefined, as here, it was manually corrected, it leaves a gap in the model that needs to be addressed. However, despite these constraints, the model could predict the shear thinning behavior better than the viscometer at a lower volume fraction.

Figure 15 illustrates the viscosity variations of the polydispersed mixture of MIL-101 (Cr) and silica nanoparticles, compared to standalone MIL-101 (Cr) and silica nanoparticles across different volume fractions and strain rates. The viscosity readings are notably high at the slowest strain rate, particularly for the mixture. This suggests that the binder and adsorbent can effectively bond at slower speeds. However, as the strain rate escalates, the viscosity decreases, indicative of shear thinning properties. This insight is valuable since the ceramic coating process relies on the adsorbent's adherence to the substrate. A static or vibrational approach can ensure optimal washcoating based on the desired volume fraction.

The monodispersed model developed heretofore could not reproduce these results because, when the silica nanoparticles occupy the interstitial space between MIL-101 (Cr) particles, a more continuous solid structure emerges, expelling liquid solvent out leading to the agglomerates that offer more resistance. More research is required to explore the modeling approaches that can cater to this effect.

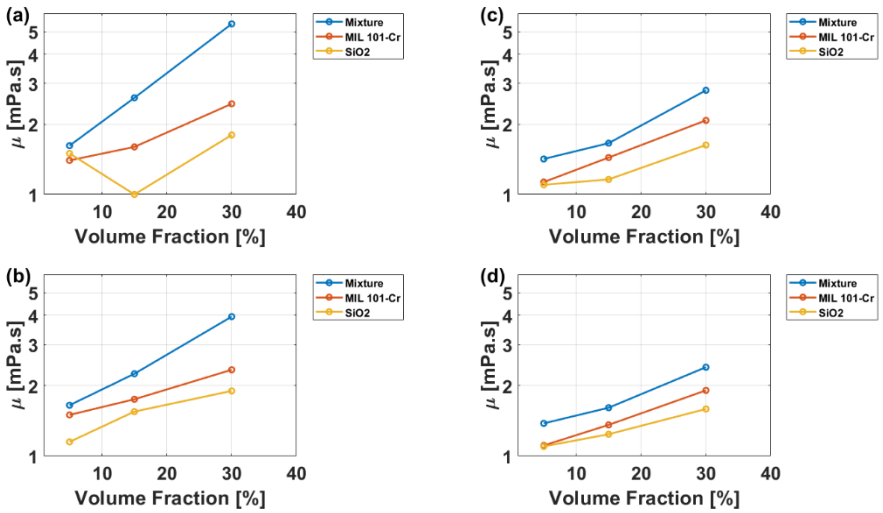

Figure 15: (a) Viscosity vs volume fraction at 6 RPM. (b) Viscosity vs. volume fraction at 12RPM. (c) Viscosity vs. volume fraction at 30 RPM. (d) Viscosity vs. volume fraction at 60 RPM for water-based slurry

3 Washcoating of Ceramic Substrates

3.1 Why Washcoating?

Packed adsorbent bed designs consisting of large adsorbent pellets (≈ 5 mm) have been conventionally used for gas separation, refrigeration, and dehydration applications. However, these structures suffer from poor heat transfer and large pressure drops across them. Due to their sluggish performance, alternative structures for adsorbent beds with miniaturized geometries like microchannels must be explored.

Commonly used structuring methods include extrusion, coating, casting, templating, thermal growth, vapor deposition, and hydrothermal transformation [28]. Among them, extrusion is the most used method due to the possibility of fabricating monolithic structures. Honeycomb monoliths of zeolites [37], ZSM-5 [38], carbon [39], and MOFs [40] have been fabricated and, in some cases, have been commercialized. The general steps are paste preparation using the adsorbent, binder, and additives; paste extrusion through the piston and die to form the desired structure; and drying and thermal treatment. The selection of the additives, such as polyethylene glycol (PEG) and methylcellulose, adds to the degrees of freedom of this process, and a trade-off between attributes like the fluidity of the solution and the strength of the product becomes inevitable. For carbon-based adsorbents, this method uses a carbon precursor, such as phenolic resin/resole, which acts as a binder and aids in the plasticity and conformity of the monolithic shape. It is then extruded to form honeycomb structures, dried, carbonized, and activated at 900°C. Such carbonization at high temperatures and cooling

leads to non-uniform shrinkage of the structure, resulting in cracks on the surface and reduced mechanical strength [41]. Gel, slip, or tape casting offers the advantage of producing the structures on a large scale [42]. While small geometrical shapes are desired for excellent heat and mass transfer attributes, the casting method is unsuitable for producing such geometries. Hollow polymeric fibers have been found to offer good transport characteristics [43], wherein a polymer binder such as Polydimethylsiloxane (PDMS) is mixed with zeolite 13X and spun into a channel shape. This method has been documented for post-combustion CO_2 capture plants; however, the process is complex and expensive. Meanwhile, binder-less methods such as hydrothermal transformation, thermal growth, and pulsed current processing (PCP) have been explored to increase adsorbent porosity. Using hydrothermal transformation, natural zeolites have been synthesized using kaolin clay [44] and glass beads [45]. All binder-less techniques require high temperatures (> 800°C) and pressure without much benefit over the low-temperature methods [46].

The washcoating or dip-coating technique is the simplest method among those explored before. Unlike the extrusion or casting methods, the coating methods rely on the geometry of the substrates. Foams [47] and honeycomb monoliths [48] are preferred substrate candidates as they offer excellent heat and mass transfer characteristics. Cordierite ceramic is typically used as the candidate material for these structures due to its low cost and low coefficient of thermal expansion (CTE). Metallic substrates have been used to perform washcoating [49]; however, thermal and chemical pretreatments of the metallic monolith are needed to improve the adhesion between the adsorbent and the substrate. Silica (SiO_2) [28] and alumina (Al_2O_3) [50] have been widely used as binders and are shown to be necessary.

Additives such as PEG are thought to improve adhesion and adsorbent loading; however, they can increase the viscosity of the slurry, which can complicate the coating process [50, 51]. MOFs, including MIL-101 (Cr), have not been washcoated onto a honeycomb of ceramic substrates before. Although zeolites have been washcoated [52], a detailed characterization of viscosity, wetting of zeolite powder with solvents, pore formation, and structural integrity is missing, and the results are based on trial and error. The washcoating process typically also involves the addition of sacrificial or pore-forming agents to create void spaces, such as yeast [53]. Additional sacrificial agents improve the diffusivity in the adsorbent layer but can hinder its mechanical strength. *Therefore, developing a thoroughly characterized washcoating process without additives or pore-forming agents becomes imperative, which becomes one of the tasks of this Thesis.*

3.2 Experimental Methodology and Results

For the washcoating process to be simple, minimum ingredients were selected for the recipe without any additives, solvents, or pore-forming agents. Cordierite honeycomb monoliths from Stanford Advanced Materials with 600 square channels per square inch (approximately 880 µm channel size with a wall thickness of 200 µm) were used (SEM image in Figure 16). Cordierite was selected because of its low cost and porous texture, which the slurry could use to form anchors for the adsorbent layer. Atomic Force Microscopy (AFM) was conducted on cordierite samples to assess the roughness of the cordierite samples. The average roughness for its surface was 0.79 µm, with peak-to-valley distance as high as 7 µm. These values indicate the potential of smaller slurry particles to occupy sites on the surface. The cordierite samples are cut into several small pieces using a diamond saw for the

washcoating experiments. A slurry was prepared using distilled water as the solvent to minimize the degrees of freedom. Water has been documented to provide excellent mechanical stability to the washcoated layers for zeolite-type adsorbents over butyl alcohol, ethyl acetate, and acetone [54]. Also, because MIL-101 (Cr) demonstrates a high affinity for water, it has the potential to be used as a pore-forming agent.

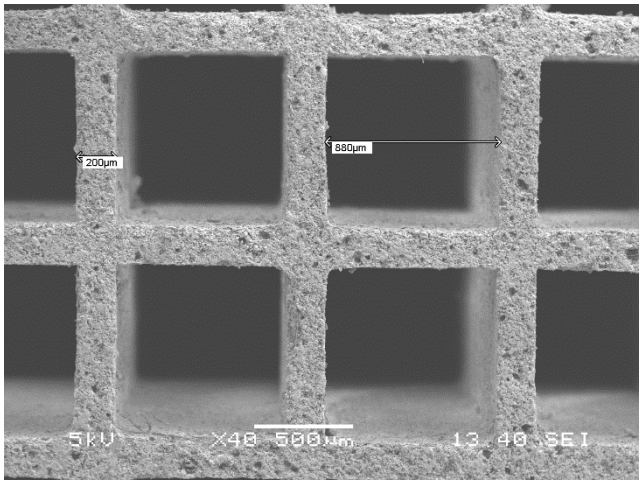

Figure 16: Uncoated cordierite honeycomb (600 channels per square inch) monolith.

First, a slurry with an initial composition of 12% MIL-101 (Cr) (procured from NanoChemazone), 3% silica binder nanopowder (SiO_2 – procured from Sky Springs Nanoparticles) in distilled water was prepared (solid particulate fraction of 15%). Note that this solid fraction does not account for the water adsorbed during slurry preparation and is thus referred to as the initial solid fraction. The solid fraction of this slurry was, in fact, on the lower end of the spectrum documented for coating zeolitic adsorbents [52]. However, the slurry was too viscous to be washcoated. This high viscosity can be attributed to the

exceptionally high water adsorption capacity combined with the hydrophilic nature of MIL-101 (Cr). The specific water adsorption capacity of MIL-101 (Cr) is at least thrice that of zeolite-13X [55], which could increase the solid fraction and, eventually, the slurry viscosity. Ultimately, decreasing the initial volume fraction below 22% yielded acceptable viscosity for the coating process.

The adsorbent mass was varied from 1 g to 5 g with a fixed silica mass of 1 g in 75 ml of distilled water. When the ingredients were mixed, the solution was homogenized using an ultrasonic bath from Cole-Parmer with a frequency of 40 kHz for three minutes. This was essential to disperse the solid particles and break bigger agglomerates into fine sizes. Afterward, the viscosity of the slurry mixture was measured using a US Solid^{TM} rotary viscometer with a resolution of 0.01 mPa-s. The solution was continuously stirred before washcoating to prevent solid particles from separating.

The washcoating of the samples was done by dipping and heating them twice (dip – heat – dip – heat). A heat gun with an air blower was employed to flash-dry the samples after dipping. The preliminary experiments used A high-pressure nitrogen blower to dry the channel walls. However, much of the coated layer was removed due to shear before it was dried, making the process redundant. This approach was documented before [56] and is not helpful when a coating layer thicker than 6 μm is desired.

Meanwhile, the coated layer was not uniform when the coated samples were kept in a tube furnace for drying without the purge gas. The adsorbent mixture showed dendritic growth, blocking the channels entirely or partially. These growths also resulted in extreme variation

in the homogeneity of the adsorbent layer across the monolith. Therefore, a heat gun, which blows high-temperature hot air at a lower velocity than the high-pressure nitrogen nozzle (~ 400°C) for a short time, was found enough to flash-dry the layer and avoid excess slurry from accumulating in the open channel area.

The samples were first weighed in weigh boats (Avogadro's Lab Supply) to begin the experiment to obtain the uncoated substrate mass and, using bulk density, the volume fraction. The sample was then dipped in the slurry for three minutes with continuous stirring to ensure that the slurry entered the channels of the samples and that no particles settled at the bottom of the glass beaker. After the first dip, the coated sample was carefully removed from the solution using forceps, considering that no channels were disturbed by them. As established earlier, a heat gun was employed at this step to flash-dry the adsorbent layer; the coated sample was kept horizontal while employing the heat gun at a temperature of 400°C to not lose any mixture due to gravity. The coated sample was then dipped in the slurry again, following the same procedure as the first dip and the first heating stage. The coated sample was then weighed again, which marks as the 'wet mass' since using a heat gun does not completely desorb and remove water; instead, it anchors the position of the solid constituents on the substrate. As found in earlier experiments, if the water desorbs from a previously dried and solidified layer, it may crack the layer. However, the heat gun shaped the layer in an annular-like fashion while not drying it entirely. After that, the water could desorb from the layer in the dedicated heating and depressurization step, making it more amenable to becoming porous.

The same procedure is repeated for the slurry samples 2 to 7 with successive additions of 1 g of MIL-101 (Cr) for the volume fraction, as shown in Table 3. Three cordierite samples were fabricated using each slurry sample. Slurry samples 2 through 5 offered no concerns while coating the cordierite channel samples. However, for the 6^{th} and the 7^{th} slurry sample, clogging was seen in the channels, which was attributed to the increased viscosity of the solution (Table 4), and using a heat gun was not enough to create a smooth annular layer. Increased surface tension could be another factor that allowed continuous menisci formation in channels. An air duster was used to eliminate clogging, which created clog-free cordierite channels.

After cordierite samples were washcoated and flash-dried using a heat gun (wet samples), their mass values were measured, which is their 'wet mass.' These samples were dried (calcinated) at 250°C in a split-tube furnace (Across International™) vacuum of 0.001 Pa for over 10 hours. This calcination was necessary to desorb all the reminiscent water from the layer while simultaneously creating passages in the layer, increasing porosity. A vacuum was necessary to avoid oxidation of the layer constituents at high temperatures, which was found to occur without a vacuum. A moisture analyzer was used to detect water removed during heating. However, because this equipment does not use vacuum conditions, cordierite samples turned dark after heating, suggesting possible oxidation, which was confirmed through FT-IR analyses. When the calcination of the coated samples was complete in the split tube furnace, the final dry mass of all samples was obtained to determine the loading.

Table 4: Test Matrix for Slurry Preparation

Slurry Number	MIL-101 (Cr) Mass [g]	SiO_2 Mass [g]	Water Mass [g]	Solid Volume Fraction [%]	Measured Slurry Viscosity [mPa-s]
1	1.00	1	75	14	3.03
2	2.00			16	4.63
3	2.50			17	5.44
4	3.00			18	6.39
5	3.50			19	7.16
6	4.00			20	7.90
7	5.00			22	9.80

3.3 Results and Discussion

3.3.1 Adsorbent Loading Analysis

The post-wash coating analysis of the samples begins with the adsorbent loading investigation. It was measured after coating, before drying in the tube furnace, and after drying in the tube furnace. Subsequently, the loading for wet and dry samples is defined in Eqs. (19) and (20).

$$Loading_{Wet} = \frac{M_{Wet,Coated} - M_{Uncoated}}{M_{Uncoated}} \times 100 \quad (19)$$

$$Loading_{Wet} = \frac{M_{Dry,Coated} - M_{Uncoated}}{M_{Uncoated}} \times 100 \quad (20)$$

Table 5 shows a calculation of the loading fractions for slurry sample 1. The table shows the dry uncoated sample mass, wet mass, and the final dry mass for three samples coated using slurry sample 1 (lowest solid fraction of 14%). As this experiment was repeated for slurry samples 2 through 7 (solid fraction 16% through 22%), similar analyses as in Table 5 were conducted to determine the wet and dry loading. The results of these loading analyses are shown in Figure 17.

Table 5: Mass and loading calculation for samples coated with slurry sample 1 (Volume Fraction 14%)

Sample	Uncoated Dry Mass [g]	Wet Mass [g]	Final Dry Mass [g]	Wet loading [%]	Dry Loading [%]
1	0.138	0.145	0.143	5.07	3.62
2	0.141	0.149	0.144	5.67	2.12
3	0.229	0.238	0.237	3.93	3.49

The wet and dry loading shows a nearly uniform increase as a function of the initial volume fraction until 19.0% (slurry sample 5). Error analyses on multiple samples prepared using the same slurry supported this observation. The loading values for the initial volume fraction of 19.0% were the highest, representing the sweet spot for these experiments and perhaps the most crucial finding reported here. As the initial solid fraction increases beyond this value, the loading values dip again. This is because of the clogging seen in multiple channels, which shows a drop in the mass of the wet and dry samples when removed using an air

duster. Regardless of the original sample mass, the adsorbent loading, as seen in Figure 18, increases almost linearly with the initial volume fraction, followed by a drop due to clearing clogs from the channel space. A couple more inferences can be drawn from these analyses.

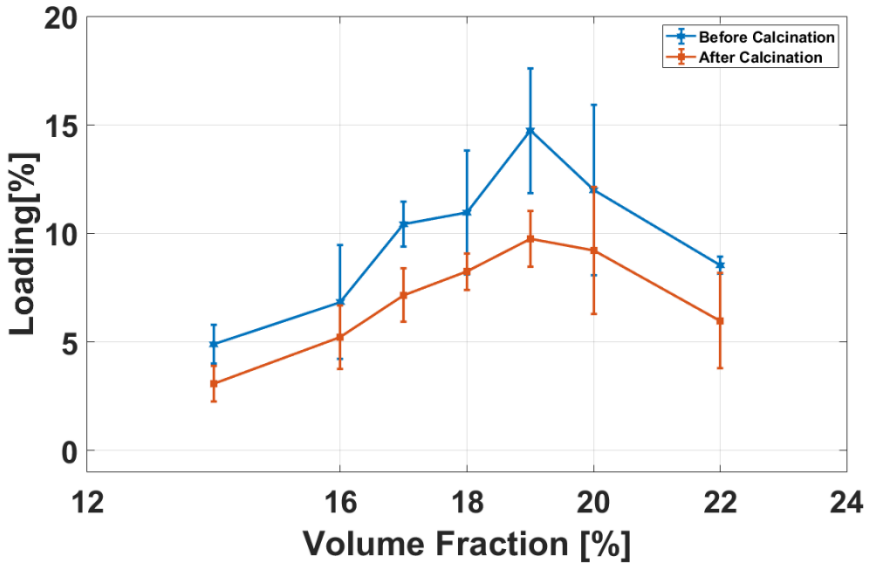

Figure 17: Wet and dry loading variation with initial solid fraction. The difference between the two represents the water desorbed during the calcination process.

First, the peak value corresponds with the binder fraction of 60% in the solid constituents (60% binder silica, 40% MIL-101 (Cr)), inferring that for every three units of binder volume, there are two units of the adsorbent, and given the size disparity, it is very much possible that the binder can effectively fill spaces between adsorbent particles, thereby improving the overall structural integrity without compromising the adsorbent functionality. As described in Table 4 and Figure 17, these curves were plotted for a constant mass of silica (13.8%),

while the adsorbent volume was increased from 2.3% to 12.71%. As explained earlier, clogging does not improve the loading of more adsorbent or solid fractions. These blocked channels end up causing severe maldistribution and underutilization of the adsorbent mass. Therefore, when these clogged channels are cleared, it is found that the binder does not hold on to the remaining adsorbent, and the layer thickness may not be predictable due loss of the solid constituents in the clogged particles.

The second factor is the amount of water desorbed during the calcination process. It becomes more evident in Figure 17 that the heat gun did not remove all the water from the adsorbent layer. The water desorbed during the final drying or calcination process can be seen in Figure 17 as the difference between the dry and wet loading. This desorbed water created void spaces in the adsorbent layer as it was removed, and a detailed SEM would help understand this effect.

3.3.2 Adsorbent Layer SEM and Image Analysis

The adsorbent layer thickness measurements using SEM and subsequent image analysis corroborated the earlier loading trend. For image analysis, avoiding parallax errors and local aggregates was essential. Therefore, the coated cordierite samples were flushed with an Epofix epoxy solution using a vacuum plate and a cylindrical cast. The epoxy solution was drawn through the cordierite channels, conforming to the shape of the adsorbent layer. The epoxy was then cured in the vacuum chamber overnight to eliminate any air bubbles and solidified. These epoxy-embedded samples were then polished using diamond polishing wheels using grit sizes of 320, 600, and 1200 and followed by superfinishing them using the

alumina solutions of 9, 6, 3, and 1 μm until the cross-sections were free of scratches. Then, these samples were taken for SEM imaging for quantitative image analysis. The samples were gold-sputtered (Denton Vacuum Desk III) on the targeted section under vacuum conditions to avoid electron charging on non-conductive cordierite and MIL-101 (Cr). The electron gun configuration in the SEM was set at 10 kV for all the samples. A sample result of epoxy-filled and polished coated channels is shown in Figure 18(a) for a 19% volume fraction. This image distinguishes between the cordierite substrate, adsorbent layer, and epoxy-filled channel area.

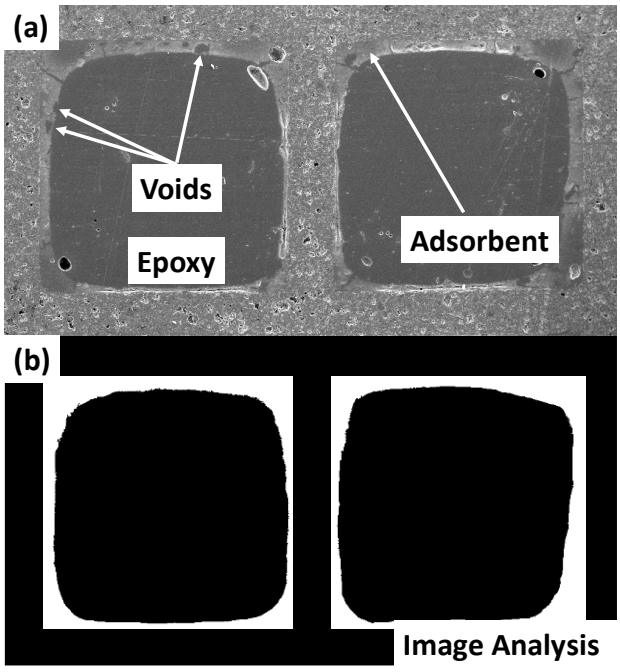

Figure 18: (a) SEM image of two channels coated with a slurry with 19% volume fraction and polishing showing the adsorbent layer and voids (b) image analysis in ImageJ and MATLAB to determine the adsorbent layer thickness.

Furthermore, the adsorbent layer shows voids, which is encouraging from the standpoint of water being used as the pore-forming agent. Meanwhile, as expected, the corners witness the adsorbent layer thickening. While a minimum thickness of 40 μm was observed on all sides of the channel, the same at corners was observed to be as high as 275 μm for some channels.

Therefore, image analyses in MATLAB were conducted to extract the quantitative adsorbent layer thickness information of every channel in the observed cross-section. Eight channels from each sample (three samples per slurry) were analyzed to obtain statistically significant information. Figure 18(b) shows a sample image analysis for the SEM images in Figure 18(a). The image analysis began with image processing. These images were processed in ImageJ to differentiate between the adsorbent and epoxy coating, as shown in Figure 18(b). A high-quality contrast between the adsorbent coating (white) and epoxy (black) was obtained through binary settings. The relative fraction of the adsorbent coating area compared to the channel area was measured in MATLAB. Then, the layer's average thickness can be determined using the known actual area of the channels. Figure 19 shows seven polished epoxy-coated samples for seven slurry samples with a solid fraction from 14% to 22%. The coating thickness could increase gradually as slurry samples became thicker and more viscous until sample 5, corresponding to a volume fraction of 19%. The coating for sample 5 is uniformly thick from all directions, with a reasonable amount of porosity in the layer. Beyond the 19% volume fraction (samples 6 and 7), the coating appears thick in some locations. However, the overall appearance is non-uniform due to the presence of clogging.

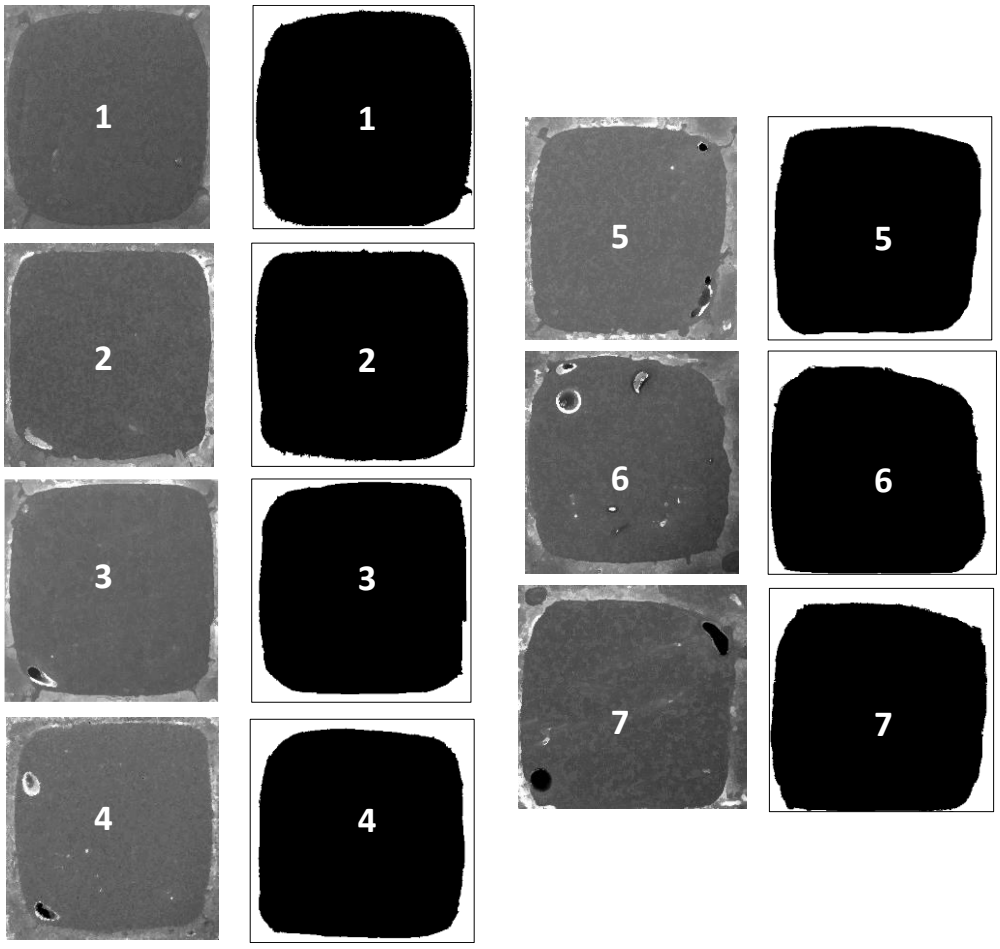

Figure 19: SEM images (left) and image analysis (right) of a single channel for slurry samples 1 to 7 described in Table 1 (14% to 22%)

The adsorbent layer thickness values determined using the image analyses are plotted in Figure 20, corroborating with the loading curves in Figure 17. The adsorbent layer thickness for the thinnest slurry is 58 ± 7μm, which increases to 106 ± 7μm for the slurry sample 5 or the sweet spot. A small standard deviation value indicated the lack of slurry flow maldistribution when coating with the slurries. After that, consistent with the loading curve, the average thickness of the layer for the slurry samples 6 and 7 was reduced to 102 ± 7 μm and 59 ± 15 μm. The high thickness variation for slurry sample 7 indicates the clogging and

irregular distribution of the adsorbent in channels during the coating process attributed to the high viscosity of the slurry sample 7.

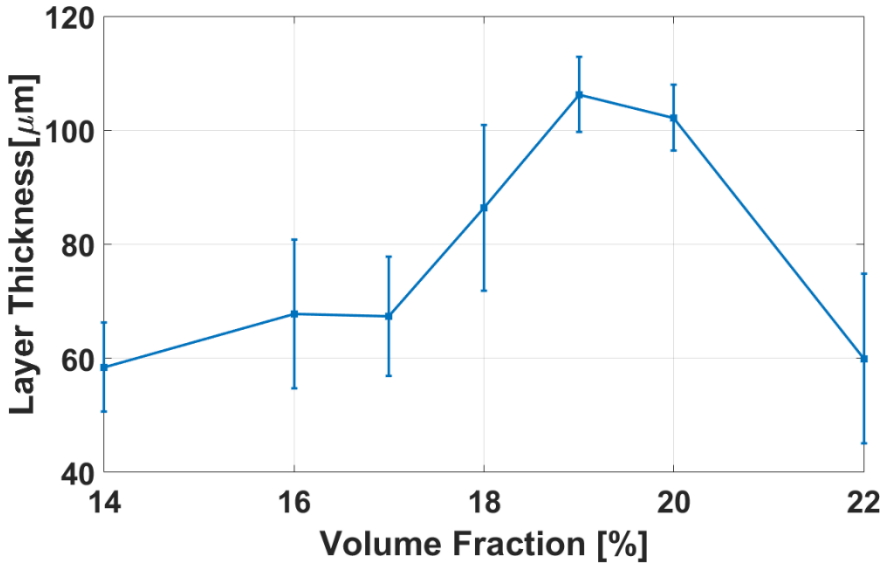

Figure 20: Variation of adsorbent layer thickness with solid fraction

3.3.3 FT-IR Analysis

The samples coated using MIL-101 (Cr) and silica binder slurry were analyzed using FT-IR (Courtesy of Dr. Sultana and Reza) to evaluate the effect of the coating process on the adsorption characteristics. As shown in Figure 21, all coated samples retain the original signature of MIL-101 (Cr) adsorbent, leading to the observation that its performance in the coated form would be retained.

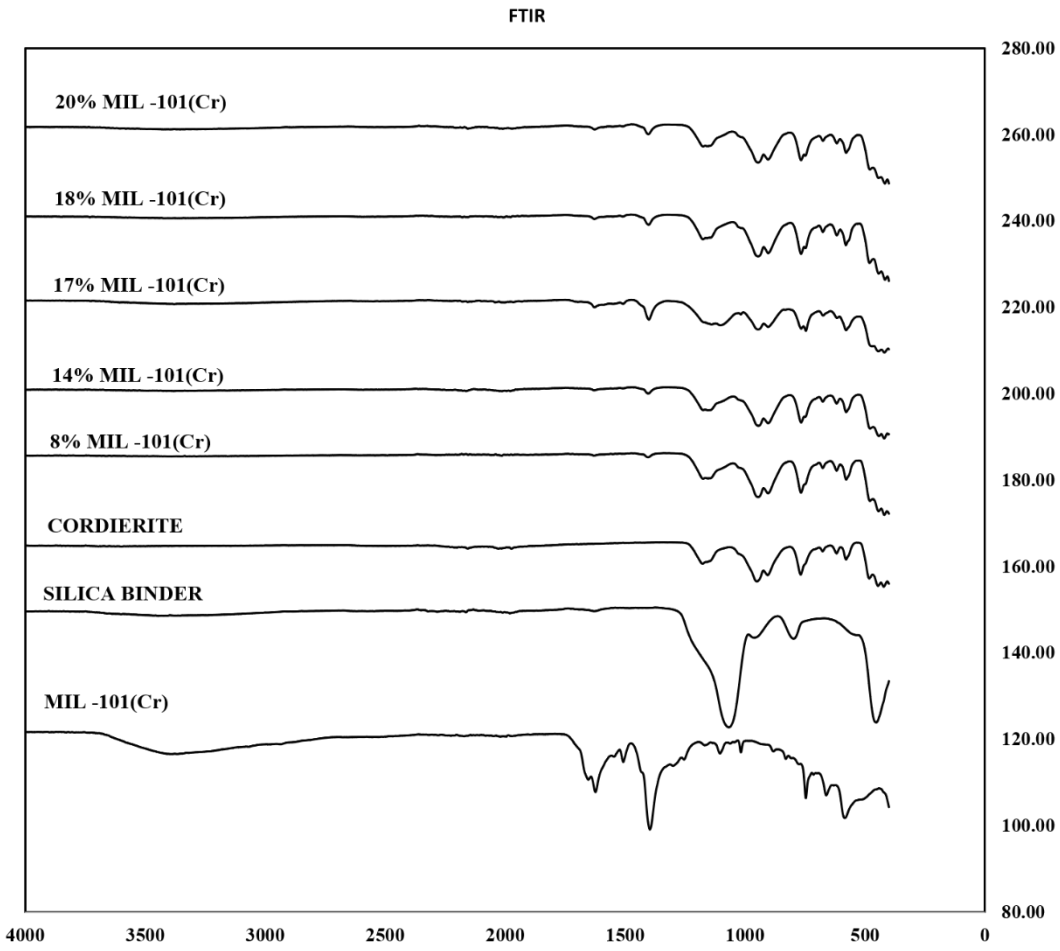

Figure 21: FT-IR spectra for MIL-101 (Cr), silica, cordierite and MIL-101 (Cr) coated samples

3.3.4 The Durability of the Coated Layer

The 21 adsorbent-coated honeycomb monolith samples prepared in this work using seven slurry samples were exposed to the ultrasonic vibration tests in the Cole-Parmer bath at 40 kHz continuously, and the individual sample weight was measured after every 400 minutes. The cordierite samples were too small to be incorporated into a setup with fluid flow to test

their endurance using that approach. Therefore, ultrasonic vibrations were utilized to test the adherence of the adsorbent layer to the cordierite samples. The samples were kept in individual glass beakers, which were kept in the bath. While the samples are expected to be kept in a pool of water in the bath, it is impossible because they would adsorb liquid water, remain wet during the entire test, and result in erroneous readings. Therefore, glass beakers isolated the bath water from the samples.

Furthermore, while voids were seen in the adsorbent layers (Figure 18), they did not become highly brittle to be disrupted by ultrasonic vibrations. Overall, strong ultrasonic vibrations did not cause a severe drop in the initial loading fraction, indicating strong adhesion between the layer and cordierite**.** The maximum loading decrease was 2.5% for **a** 22% volume fraction (20% MIL-101 (Cr)).

Thinner slurries resulted in lower loading values and a flatter or more favorable loading endurance curve. Meanwhile, the samples with higher loading values showed a more steady and gradual drop because of the availability of more adsorbent particles to release in the ultrasonic bath. In particular, as expected, the attrition rate was proportional to the original loading fraction, as seen in Figure 17.

Figure 22 shows that the adsorbent layer was strong enough to continuously withstand the 40 kHz ultrasonic vibrations for more than 4800 minutes. Further analysis of the porosity investigation and its dependence on the vibration tests would quantify this relationship comprehensively.

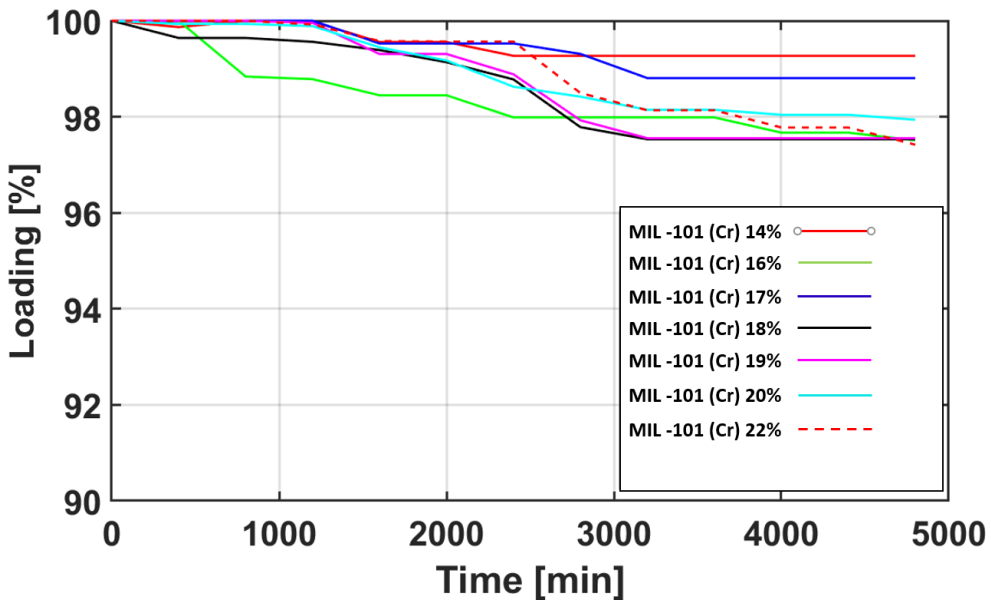

Figure 22: Particle attrition as a function of slurry (or MIL-101 (Cr)) solid fraction

3.4 Water Adsorption Tests

While the samples showed good adhesion performance when subjected to ultrasonic vibrations, their cyclic water uptake must be investigated to ensure that the MIL-101 (Cr) adsorbent pore structure would sustain cyclic water adsorption and desorption. Because these samples were made from cordierite ceramic to demonstrate the coating method, they cannot be used as channels in a closed or sealed system. Therefore, the samples must be exposed to the adsorbate vapor in a controlled setting like a glass tube. A benchtop uptake setup was constructed, as shown in Figure 23, which shows a cylinder filled with distilled water, a needle valve

to control the water evaporation, a tube furnace with a vacuum pump, and high sensitivity (± 10 Pa) Alicat pressure sensor.

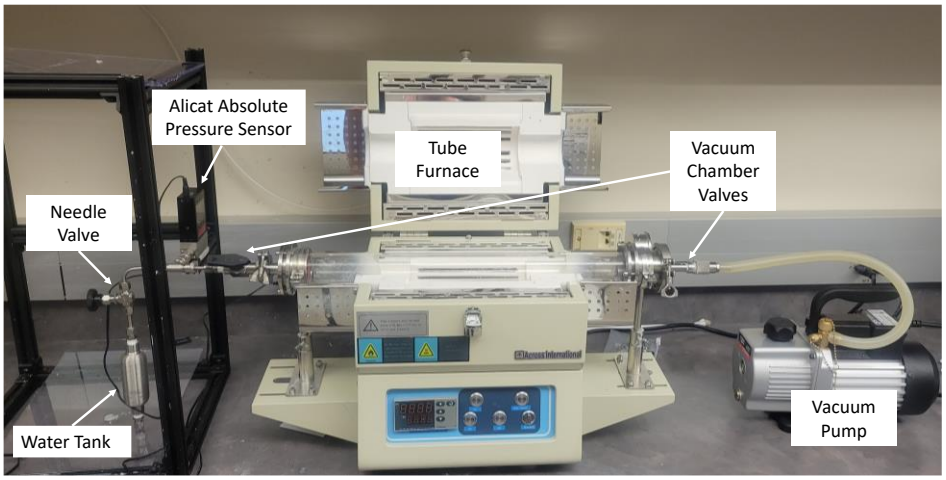

Figure 23: Adsorbent uptake setup constructed for water adsorption in cordierite samples

Fourteen samples fabricated from the seven slurry samples (two samples per slurry), as described in earlier sections, were used for the water uptake experiments. The procedure started with calcinating all samples for 12 hours at 200℃ in the tube furnace with the vacuum pump running. Afterward, the samples were taken out of the furnace and weighed quickly (to avoid atmospheric water vapor entering them) within the error margin of ± 0.1 mg, indicating their dry initial mass. These samples were kept in the glass tube; all valves except the needle valve to the water cylinder were opened, and the vacuum pump was started. When a vacuum was created in the tube, the vacuum chamber outlet valve to the pump was closed. The vacuum chamber

would be leakproof if the vacuum pressure were maintained. Then, the needle valve to the liquid water was opened, causing the water to evaporate under vacuum pressure. The vapor entering the glass tube increased the saturation pressure to 2.65 kPa within a few seconds at room temperature, which was maintained at 22℃. At this pressure, the valve to the tank was closed, and the pressure in the tube decreased again, reaching as low as 1.8 kPa, indicating that the dry samples were still adsorbing water vapor. When the needle valve was opened again, the pressure increased back to 2.65 rapidly due to evaporation. Then the valve was closed again, leading to a drop in pressure due to continued adsorption. Eventually, the pressure decrease after the needle valve closure was no longer observed when the samples were saturated with water.

When the needle valve was opened, condensation was observed on the inner wall of the glass tube, and the pressure reading kept fluctuating around 2.65 kPa, indicating that the condensation on the walls was compensating for evaporation in the tank. The adsorption experiment was stopped, and the samples were taken out and weighed again. The difference between this mass and the dry initial mass indicated the amount of water adsorbed during the experiment for each sample. Then, all samples were calcinated again for 12 hours at 200℃ with the vacuum pump running, followed by the adsorption experiment described earlier. This experiment was conducted for five such cycles, shown in **Figure 24**.

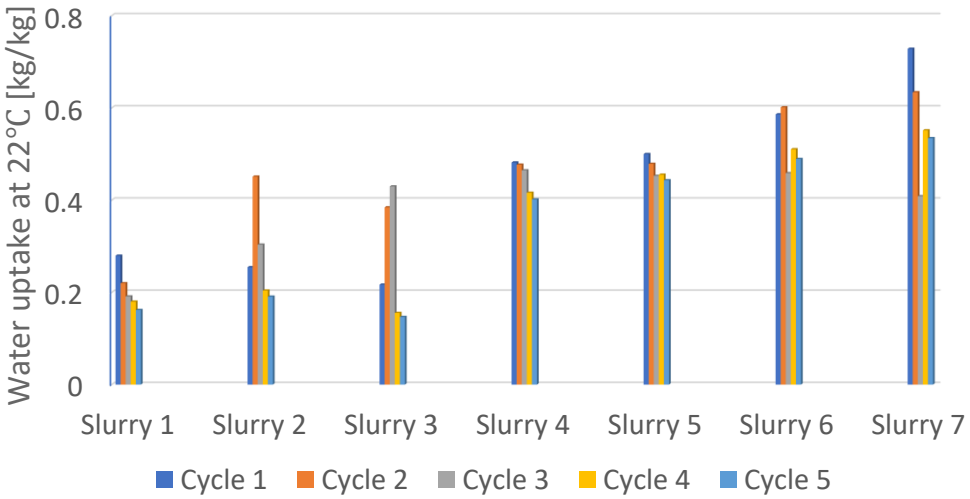

Figure 24: Average water vapor uptake for two coated samples. Fourteen samples prepared using seven different slurries as described in earlier sections were used.

Figure 24 shows two interlinked trends of water uptake fraction as a function of solid fraction (slurries of different MIL-101 (Cr) fractions) and as a function of successive adsorption/desorption cycles. First, as the solid fraction increased, the average water uptake gradually increased from 20% to 57% for all cycles. This is consistent with the understanding that the increased MIL-101 (Cr) in the samples prepared using thicker slurries adsorbed more water. Meanwhile, no distinct pattern was observed in the water uptake for individual slurry samples for successive adsorption and desorption. While slurry samples #1, 4, and 5 showed a gradual drop of 35%, 13%, and 9% between the first and fifth cycles, respectively, this decreasing trend of water uptake with the increasing slurry solid fraction (35% to 9%) is not consistent with any other variable. Meanwhile, the other samples showed no distinct

trend between the first and fifth adsorption/desorption cycles. There could be several reasons for this outcome, as follows:

The gravimetric uptake measurements performed on open samples, as prepared in this work, are subject to randomness in cutting the cordierite samples and their orientation when in the glass tube. In particular, when the samples have only internal walls without any peripheral support wall, the adsorbent loading is smaller than the sample when it has a covering wall. Note that the entire surface is coated in this dip coating or washcoating approach, not just the internal walls. Considering that the samples were taken out of the vacuum conditions to measure their mass, and experiments were conducted on different days with a possible change in specific humidity, the sample orientation in the tube furnace may have played a role in the water uptake in every cycle, yet, they have retained significant adsorption capacity after five cycles.

It has been reported in a study that iron-deposited MIL-101 (Cr) may lose its ability to adsorb after a few cycles because of crystal structure collapse [57]. This was likely due to iron deposition on the adsorbent, exacerbated at temperatures 110℃-150℃, as evidenced by the XRD plots. Some solvents may degrade its performance as well. Nevertheless, the study reports a better stability performance for MIL-101 (Cr) than other adsorbents. In another study, a standalone MIL-101 (Cr) adsorbent-packed bed column showed an excellent cyclic CO_2 adsorption capacity after regeneration for five cycles [58].

The Brunauer–Emmett–Teller (BET) specific surface area (SSA) of the 'as received' MIL-101 (Cr) was measured using Micromeritics High-Pressure Volumetric Analyzer (II) using the procedure described in an earlier article (Courtesy Dr. Sultana and Dr. Reza), and the value was found to be 1320 m^2 g^{-1}. Some of this MIL-101 (Cr) powder was then calcinated at 200℃ under vacuum for 18 hours, and the BET SSA was measured again, and surprisingly it was found to be 1562 m^2 g^{-1}, which shows that calcination does not affect the BET area or the structure it opens the pores, removes some more moisture that results in slightly higher BET area than the 'as received samples. However, FT-IR measurements shown in Figure 25 show a strong transmittance signature for MIL-101 (Cr) in coated samples. Therefore, the samples used in the cyclic water adsorption experiments were reanalyzed afterward with FT-IR, and the results are shown in Figure 25. The MIL-101 (Cr) peaks are visible, as shown in the blue oval, like those seen in Fig. 9 for samples before any water uptake experiments but after fabrication. The transmittance profiles for these five samples are commensurate with the adsorbent fraction shown in Figure 25. These peaks show that the adsorbent has retained its properties and shows a presence corresponding to its fraction in the samples. Figures 24 and 25 show that the adsorbent properties do not significantly deteriorate after five adsorption and desorption cycles for water. It should also be noted that the temperature at which these samples are regenerated after adsorption is significantly high (200℃).

Nevertheless, there must be insignificant damage to the MIL-101 (Cr) structure in successive cycles that allowed them to maintain the water uptake for most cases.

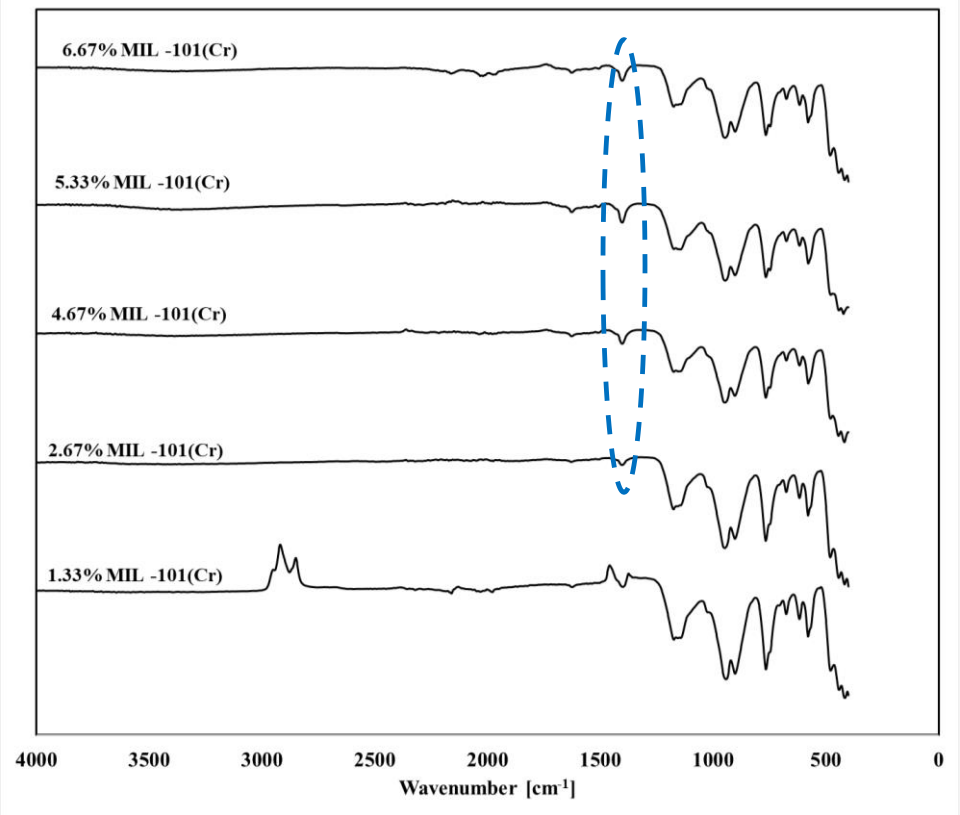

Figure 25: FT-IR spectra for MIL-101 (Cr) coated samples after five cyclic water uptake measurements.

4 Conclusion

The highlights of this thesis are listed in this chapter. As delineated in Chapter 1, this thesis focuses on (a) understanding the properties of adsorbent slurries, particularly viscosity, and (b) developing a novel washcoating process for MIL-101 (Cr) adsorbent with the knowledge gained from the viscosity study.

The viscosity of adsorbent slurries depends on parameters such as particle size, density, strain rate, adsorption capacity, wetting and adsorption, volume fraction and liquid-solid contact angle. Notably, ethanol slurries exhibit a higher viscosity than those made with distilled water. Moreover, the developed semi-empirical model could determine viscosity using the contact angle, highlighting the importance of wetting phenomena in understanding the rheological behavior of slurries, regardless of solute porosity. Leveraging these viscosity insights, a novel method for coating ceramic substrates is developed. Optimal loading was observed at a 19% volume fraction mixture for MIL-101 (Cr) and silica binder in a water-based slurry. This volume fraction and the solvent can be adjusted based on the substrate's surface and the loading goals. An important observation was the shear thinning behavior for all slurries, indicating coatings can be applied in either a stationary or vibrating mode to optimize adsorbent adherence. A specific summary from each of these chapters is as follows:

4.1 Unified Model for Viscosity

Experiments were conducted to determine the viscosities of porous solutes (MIL-101 (Cr), silica nanoparticles, titania) and non-porous solutes (glass beads) in solvents such as water

and ethanol. Their rheological behavior was then assessed to identify patterns and the factors affecting overall viscosity. It was observed that, regardless of porosity, all the slurries displayed shear thinning behavior, especially at high-volume fractions. A significant observation was the increased viscosity of all the solutes in ethanol, which can be attributed to the low contact angle permitted between ethanol and solute particles, promoting enhanced wetting. As a result, superior wetting in ethanol slurries leads to a more pronounced increase in viscosity than water-based slurries at the same volume fractions.

The model optimizes the volume fraction by factoring in adsorption for porous solutes. The optimized 0.1 exponent value associated with the volume fraction accounts for the rise in volume fraction and, consequently, the overall viscosity. Since the number of particles increases with the volume fraction, the model must account for this change; therefore, a ratio (the number of water molecules to the number of particles) was determined, and its value was found to be 1, indicating a linear relationship. Moreover, the size of the particle significantly influences the viscosity, particularly when considering different solvents. Thus, the model incorporates this variation by associating its exponent with its density, strain rate, and the solvent's viscosity, allowing for a more comprehensible observation. The contact angle between the particles of solutes and solvents plays a crucial role in determining viscosity because wetting is important. Therefore, when it is integrated into the model, the accuracy increases. However, since the experiment to determine this contact angle is yet to be conducted, it was excluded from the MATLAB optimization process to avoid inaccuracies in the model.

Upon assessing the slurry of MIL-101 (Cr), silica nanoparticles, and water, it was found that the viscosity was higher compared to slurries with individual solutes. This increase can be attributed to polydispersity and the interaction between MIL-101 (Cr) and silica nanoparticles, where silica particles bind with the MIL 101-Cr particles. This underscores the potential of exploiting surface area and wetting phenomena, especially when preparing slurries for washcoating applications. From these observations and data, parameters influencing the rheological behavior of the slurries were identified, and a dimensionless analysis was performed using the Buckingham Π theorem. Subsequently, a semi-empirical model was developed and optimized using a genetic algorithm in MATLAB. To assess the model's accuracy, it was tested for 20% and 30% volume fractions, and the results were found to align closely with experimental values. However, for the model to be entirely precise, it's essential to integrate further parameters, such as variations in temperature, the shape of particles, and experimentally measured contact angles. These adjustments will be addressed in the future.

4.2 Washcoating MIL-101 (Cr) on Cordierite

A novel washcoating method was developed for fabricating the MIL-101 (Cr) coated adsorbent layer on cordierite honeycomb monolith. The method included using distilled water as the solvent, silica nanopowder as the binder, and MIL-101 (Cr) powder as the adsorbent. Because water has a very high affinity for MIL-101 (Cr), it was used as a pore-forming agent, which precludes using any dedicated pore-forming agent, and it is one of the major highlights of this work. The steps included mixing these ingredients to prepare the slurry, dipping the cordierite samples into the slurry, and heating and drying the samples at

250°C in a vacuum-assisted tube furnace. This process was optimized based on the preliminary experiments and observations. The major conclusions from the study are as follows:

A sweet spot of 10% adsorbent loading was observed for a solid fraction of 19% when it was varied from 14% to 22% with a fixed binder concentration of 1.33%. This corresponds to the adsorbent-to-binder ratio of 4 and indicates the binding capacity of silica nanopowders. The smaller MIL-101 (Cr) fraction was favorable for the binder. However, the viscosity of the slurry was too small to allow any particulate retention. As the slurry viscosity increased, the retention increased, allowing a thicker layer to develop without clogging. Further increase in the MIL-101 (Cr) resulted in even more thick slurries; however, clogging occurred in the channels with irregular loading patterns. The loading value decreased when these clogs were removed, giving rise to a preferred volume fraction of 19%.

The image analyses of the cordierite samples were conducted using SEM, ImageJ, and MATLAB to calculate the average adsorbent layer thickness and assess adsorbent maldistribution. Slurry samples 1 to 5 (14% to 19% solid fraction) indicated a gradual increase in the adsorbent layer thickness from 58 μm to 106 μm, consistent with the loading curve. In comparison, the standard deviation in the adsorbent layer thickness was consistently slight for slurry samples 1 to 6 (14% to 19% solid fraction), indicating insignificant maldistribution of the coating process. The SEM images of different samples confirmed the presence of void fractions and uniform adsorbent layers for the slurries until the sweet spot. Meanwhile, the loading and the adsorbent layer thickness decreased for the

thickest slurry (22% solid fraction) because of significant clogging and maldistribution, which is not preferable despite high initial retention.

The FT-IR analyses conducted on pure cordierite, pure silica, pure MIL-101 (Cr), and coated samples confirmed that no significant change in the MIL-101 (Cr) properties occurred due to the coating process. The adsorbent properties were well represented in the coated and pure forms. Meanwhile, the effect of increasing the adsorbent fraction was observed in the transmittance analyses using FT-IR. While these results are to be confirmed using breakthrough and separation studies, it can be claimed that the adsorbent properties remain unaltered after the coating process due to its simplicity.

Finally, the adsorbent layers fabricated using this method were highly durable and capable of withstanding the ultrasonic vibrations at 40 kHz for more than 4800 hours. After this period, a maximum drop of 2.5% in the initial loading was observed. This indicates good adhesion between the adsorbent layer and cordierite substrates, which is also confirmed by the SEM images through no gaps or delamination. The presence of void spaces was found not to affect the strength of the layer, and their presence in the adsorbent layer confirmed the creation of void space without using pore-forming agents.

The coated samples showed an excellent water uptake performance at 22℃ for five consecutive cycles, which were regenerated at 200℃ for 12 hours under vacuum. This gravimetric approach shows a nominal drop in the water uptake for all slurry samples, consistent with the literature. Considering the challenges that the samples were taken out of the vacuum conditions into the atmospheric conditions to measure their mass, experiments

were conducted on successive days with a possible change in specific humidity; the sample orientation in the tube furnace may have played a role in the water uptake in every cycle, yet they have retained their adsorption capacity after five cycles. It can also be safely inferred that the adsorbent signature was retained after five uptake cycles in the FT-IR measurements. An accurate analysis of water uptake is currently ongoing using breakthrough analyses, where the volumetric uptake approach would yield a more accurate result without exposure to atmospheric humidity. The BET SSA measurements on the standalone powders 'as received' vs. calcinated at 200℃ were 1320 and 1562 m^2 g^{-1}, respectively, which showed that calcination does not change the adsorbent structure; it opens more pores, where atmospheric water vapor might have been adsorbed resulting in this increase in the BET area.

While these results are significant, a detailed study on the characterization of the adsorbent slurry through viscosity models and the adsorbent porosity analyses through tomographic analyses would result in a comprehensive understanding of this washcoating process, which does not use pore-forming agents.

Further work is required to enhance the model's precision and actual time application for the washcoating process. For this, the future work entails factoring in elements such as temperature and zeta potential and evaluating viscosity at all strain rates with every iteration being captured. This ensures a comprehensive understanding of the slurries' rheology and their use in different applications.

5 References

1. Pahinkar, D.G. and S. Garimella, *Experimental and computational investigation of gas separation in adsorbent-coated microchannels.* Chemical Engineering Science, 2017. **173**: p. 588-606.
2. Pahinkar, D.G. and S. Garimella, *A novel temperature swing adsorption process for natural gas purification, Part II: Performance assessment.* Separation and Purification Technology, 2018. **204**: p. 81-89.
3. Pahinkar, D.G. and S. Garimella, *A novel temperature swing adsorption process for natural gas purification: Part I, model development.* Separation and Purification Technology, 2018. **203**: p. 124-142.
4. Hamamoto, Y., et al., *Performance evaluation of a two-stage adsorption refrigeration cycle with different mass ratio.* International Journal of Refrigeration, 2005. **28**(3): p. 344-352.
5. Meunier, F., *Adsorption heat powered heat pumps.* Applied Thermal Engineering, 2013. **61**(2): p. 830-836.
6. San, J.-Y. and F.-K. Tsai, *Testing of a lab-scale four-bed adsorption heat pump.* Applied Thermal Engineering, 2014. **70**(1): p. 274-281.
7. Pahinkar, D.G., D.B. Boman, and S. Garimella, *High performance microchannel adsorption heat pumps.* International Journal of Refrigeration, 2020. **119**: p. 184-194.
8. Ko, N., et al., *Tailoring the water adsorption properties of MIL-101 metal–organic frameworks by partial functionalization.* Journal of Materials Chemistry A, 2015. **3**(5): p. 2057-2064.
9. Soliman, A., et al., *A Review on New 3-D Printed Materials' Geometries for Catalysis and Adsorption: Paradigms from Reforming Reactions and CO2 Capture.* Nanomaterials, 2020. **10**(11).
10. Zhao, H., et al., *Synthesis of MIL-101(Cr) and its water adsorption performance.* Microporous and Mesoporous Materials, 2020. **297**: p. 110044.
11. Foundation, C.-. *Biochemical Properties of Water - Advanced*. [cited 2022 05-19-2022]; Available from: https://www.ck12.org/biology/structure-and-properties-of-water/lesson/Biochemical-Properties-of-Water-Advanced-BIO-ADV/.
12. Viswanath, D.S., et al., *Viscosity of Liquids: Theory, Estimation, Experiment, and Data*. 1 ed. 2007: Springer Dordrecht. 662.
13. Pal, R., *New Generalized Viscosity Model for Non-Colloidal Suspensions and Emulsions.* Fluids, 2020. **5**(3).
14. Einstein, A., *Eine neue bestimmung der moleküldimensionen*. 1905, ETH Zurich.
15. Rutgers, I.R., *Relative viscosity and concentration.* Rheologica Acta, 1962. **2**(4): p. 305-348.
16. Pal, R., *New Generalized Viscosity Model for Non-Colloidal Suspensions and Emulsions.* Fluids, 2020. **5**(3): p. 150.
17. Krieger, I.M. and T.J. Dougherty, *A Mechanism for Non-Newtonian Flow in Suspensions of Rigid Spheres.* Transactions of The Society of Rheology, 1959. **3**(1): p. 137-152.
18. Pal, R., *New Models for the Viscosity of Nanofluids.* Journal of Nanofluids, 2014. **3**(3): p. 260-266.

19. Thomas, D.G., *Transport characteristics of suspension: VIII. A note on the viscosity of Newtonian suspensions of uniform spherical particles.* Journal of Colloid Science, 1965. **20**(3): p. 267-277.
20. Konijn, B.J., O.B.J. Sanderink, and N.P. Kruyt, *Experimental study of the viscosity of suspensions: Effect of solid fraction, particle size and suspending liquid.* Powder Technology, 2014. **266**: p. 61-69.
21. Kurgaev, E.F., *On the viscosity of suspensions.* Doklady Akademii Nauk SSSR, 1960. **132**(2): p. 392-394.
22. Jirgensons, B. and M.E. Straumanis, *CHAPTER 4 - THE KINETIC PROPERTIES OF DISPERSE SYSTEMS*, in *A Short Textbook of Colloid Chemistry (Second Edition)*, B. Jirgensons and M.E. Straumanis, Editors. 1962, Pergamon. p. 33-45.
23. Beltrán, A., et al., *Experimental study of the effect of wettability on the relative permeability for air–water flow through porous media.* International Journal of Multiphase Flow, 2019. **120**: p. 103091.
24. Jarrah, A. and S. Farhadi, *Dawson-Type Polyoxometalate Incorporated into Nanoporous MIL-101(Cr): Preparation, Characterization and Application for Ultrafast Removal of Organic Dyes.* Acta Chimica Solvenica, 2019. **66**(1).
25. Kim, K.M., et al., *Surface treatment of silica nanoparticles for stable and charge-controlled colloidal silica.* Int J Nanomedicine, 2014. **9 Suppl 2**(Suppl 2): p. 29-40.
26. YU Ying, S.X., YAN Jian, XIAO Jing, XI Hongxia, LI Zhong, *Adsorption equilibrium and mechanism of ethanol on MIL-101(Cr).* CIESC Journal, 2016. **67**(1): p. 300-308.
27. Chauhan, N., et al., *Synthesis and Characterization of MIL–101 (Cr) Adsorbent Coating on Microchannel Walls for Water Adsorption Heat Pumps.* Industrial & Engineering Chemistry Research, 2022. **61**(39): p. 14573-14585.
28. Akhtar, F., et al., *Structuring adsorbents and catalysts by processing of porous powders.* Journal of the European Ceramic Society, 2014. **34**(7): p. 1643-1666.
29. *Titanium Oxide Nanoparticles/ Nanopowder (TiO2) anatase, 5nm*. 2023, SkySpring Nanomaterials.
30. *Silicon Oxide Nanoparticles/ Silicon Oxide Nanopowder (SiO2) 99.5%, 10~20nm*. 2023, SkySpring Nanomaterials.
31. Jirgensons, B. and M.E. Straumanis, *CHAPTER 2 - CLASSIFICATION OF COLLOIDS. THE BASIC TERMS IN COLLOID CHEMISTRY*, in *A Short Textbook of Colloid Chemistry (Second Edition)*, B. Jirgensons and M.E. Straumanis, Editors. 1962, Pergamon. p. 8-18.
32. Ethington, E.F., *Interfacial contact angle measurements of water, mercury, and 20 organic liquids on quartz, calcite, biotite, and Ca-montmorillonite substrates*, D.o. Interior, Editor. 1990: Golden CO.
33. Mo-Sci, *Soda Lime Glass Spheres*. 2023.
34. Zaib, Q., M. Jouiad, and F. Ahmad, *Ultrasonic Synthesis of Carbon Nanotube-Titanium Dioxide Composites: Process Optimization via Response Surface Methodology.* ACS Omega, 2019. **4**(1): p. 535-545.
35. Fazio, G., et al., *Curved TiO2 Nanoparticles in Water: Short (Chemical) and Long (Physical) Range Interfacial Effects.* ACS Applied Materials & Interfaces, 2018. **10**(35): p. 29943-29953.
36. MathWorks, *gamultiobj*, in *MathWorks Documentation*. 2022, MathWorks

37. Zacahua-Tlacuatl, G., et al., *Rheological Characterization and Extrusion of Suspensions of Natural Zeolites.* Applied Rheology, 2010. **20**: p. 26 - 35.
38. Aranzabal, A., et al., *Optimization of process parameters on the extrusion of honeycomb shaped monolith of H-ZSM-5 zeolite.* Chemical Engineering Journal, 2010. **162**(1): p. 415-423.
39. Gadkaree, K.P., *Carbon honeycomb structures for adsorption applications.* Carbon, 1998. **36**(7): p. 981-989.
40. Hong, W.Y., S.P. Perera, and A.D. Burrows, *Manufacturing of metal-organic framework monoliths and their application in CO2 adsorption.* Microporous and Mesoporous Materials, 2015. **214**: p. 149-155.
41. Vergunst, T., et al., *CARBON-BASED MONOLITHIC STRUCTURES.* Catalysis Reviews, 2001. **43**(3): p. 291-314.
42. Wang, H., et al., *Hierarchical zeolite structures with designed shape by gel-casting of colloidal nanocrystal suspensions.* Chemical Communications, 2001(15): p. 1364-1365.
43. Lively, R.P., et al., *Hollow Fiber Adsorbents for CO2 Removal from Flue Gas.* Industrial & Engineering Chemistry Research, 2009. **48**(15): p. 7314-7324.
44. Pavlov, M.L., et al., *Binder-free syntheses of high-performance zeolites A and X from kaolin.* Petroleum Chemistry, 2009. **49**(1): p. 36-41.
45. Scheffler, F., et al., *Transformation of porous glass beads into MFI-type containing beads.* Microporous and Mesoporous Materials, 2002. **55**(2): p. 181-191.
46. Moreno-Castilla, C. and A.F. Pérez-Cadenas, *Carbon-Based Honeycomb Monoliths for Environmental Gas-Phase Applications.* Materials, 2010. **3**(2).
47. Yanase, I., Y. Yamakawa, and H. Kobayashi, *CO₂ absorption of CaO coated on aluminosilicate foam.* Journal of the Ceramic Society of Japan, 2008. **116**(1350): p. 176-180.
48. Liu, Q., et al., *Al2O3-Coated Honeycomb Cordierite-Supported CuO for Simultaneous SO2 and NO Removal from Flue Gas: Effect of Na2O Additive.* Industrial & Engineering Chemistry Research, 2004. **43**(15): p. 4031-4037.
49. Wu, D., Y. Zhang, and Y. Li, *Mechanical stability of monolithic catalysts: Improving washcoat adhesion by FeCrAl alloy substrate treatment.* Journal of Industrial and Engineering Chemistry, 2017. **56**: p. 175-184.
50. Kong, X., et al., *Influence of alumina binders on adhesion and cohesion during preparation of Cu-SAPO-34/monolith catalysts.* International Journal of Applied Ceramic Technology, 2018. **15**(6): p. 1490-1501.
51. Edgar-Beltran, A., et al., *Improving Adhesion and Coating Integrity of Washcoat and Overcoats* 2010.
52. Mitra, B. and D. Kunzru, *Washcoating of Different Zeolites on Cordierite Monoliths.* Journal of the American Ceramic Society, 2008. **91**(1): p. 64-70.
53. Dhillon, P.S., et al., *Enhanced transport in washcoated monoliths: Application to selective lean NOx reduction and ammonia oxidation.* Chemical Engineering Journal, 2019. **377**: p. 119734.
54. Zamaro, J.M., M.A. Ulla, and E.E. Miró, *The effect of different slurry compositions and solvents upon the properties of ZSM5-washcoated cordierite honeycombs for the SCR of NOx with methane.* Catalysis Today, 2005. **107-108**: p. 86-93.

55. Son, K.N., T.-M.J. Richardson, and G.E. Cmarik, *Equilibrium Adsorption Isotherms for H2O on Zeolite 13X*. Journal of Chemical & Engineering Data, 2019. **64**(3): p. 1063-1071.
56. Truter, L.A., et al., *Metal–Organic Framework Capillary Microreactor for Application in Click Chemistry.* ChemCatChem, 2016. **8**(9): p. 1692-1698.
57. Zhuang, H., et al., *Vapor Deposition-Prepared MIL-100(Cr)- and MIL-101(Cr)-Supported Iron Catalysts for Effectively Removing Organic Pollutants from Water.* ACS Omega, 2021. **6**(39): p. 25311-25322.
58. Liu, Q., et al., *Adsorption of Carbon Dioxide by MIL-101(Cr): Regeneration Conditions and Influence of Flue Gas Contaminants.* Scientific Reports, 2013. **3**(1): p. 2916.